Supporting Information for "New Insights into the Radical Chemistry and Product Distribution in the OH-initiated Oxidation of Benzene"

Lu Xu,*,† Kristian H. Møller,‡ John D. Crounse,† Henrik G. Kjaergaard,‡ and Paul O. Wennberg*,†,¶

†*Division of Geological and Planetary Sciences, California Institute of Technology, Pasadena, California 91125, United States*

‡*Department of Chemistry, University of Copenhagen, Universitetsparken 5, DK-2100 Copenhagen Ø, Denmark*

¶*Division of Engineering and Applied Science, California Institute of Technology, Pasadena, California 91125, United States*

E-mail: luxu@caltech.edu; wennberg@caltech.edu

This PDF file includes

S1: Experimental Conditions

Benzene (99.8% Sigma-Aldrich), CH_3ONO (synthesized following Taylor et al.[1]), and NO (1993±20 ppmv, Matheson) are injected into the chamber in a similar fashion. Briefly, the standard is firstly introduced to an evacuated gas-tight 500 cm^3 glass bulb, and then undergoes serial dilution with N_2 to achieve the desired mixing ratio. The analyte in the glass blub is quantified by FTIR spectroscopy using tabulated cross section and then injected into the chamber. 8 UV lights (Sylvania F40/350BL) are used. The measured j_{CH_3ONO} and inferred j_{NO_2} are 1.1×10^{-3} s^{-1} and 4.4×10^{-3} s^{-1}, respectively. The experimental conditions are summarized in Table S1.

Table S1: Experimental conditions.

Expt No.	initial concentration (ppb)				Ox Time (min)	[OH][b] ($\times10^8$)	Δ[Benzene] (ppb)	note
	Benzene	OH source[a]	NO	NO_2				
1	785	2000	0	0	2400	0.033	55	
2	1473	501	4673	300	52	0.11	53	
3	1525	542	1225	60	12	0.62	61	
4	1456	557	593	19	12.5	1.14	100	
5	1446	527	289	10	6.5	1.54	100	
6	1509	525	168	5	5	1.61	108	
7	1428	537	35	1	5.5	1.72	121	
8	1487	509	0	0	7	1.79	128	c
9	1422	568	0	0	7	1.71	112	d
10	1463	576	2100	127	30	0.21	67	d
11	1429	490	0	0	40	0.21	98	d,e
12	1408	492	729	17	12	0.65	80	d
13	1580	517	727	28	12	0.73	92	d

[a] H_2O_2 is used as OH source for Expt 1 and CH_3ONO is used as OH source for all other experiments.

[b] unit: molecule cm^{-3}. Determined from the measured decay rate of benzene.

[c] Continuous injection of isotopically labeled benzene (benzene-d_6, 99%, Sigma Aldrich) with constant concentration into the CIMS, to better quantify the reaction amount of benzene in the reaction chamber. However, benzene-d_6 is an isobaric compound of $C_4H_4O_2$ and interferes the quantification of $C_4H_4O_2$.

[d] GC column condition changed so that the chromatograms can only be compared between experiments 9-13, not with experiments 1-8.

[e] Only one light bulb is used.

S2: CIMS operation and sensitivity

The CIMS is operated in two alternating modes: negative mode with CF_3O^- as reagent ion and positive mode with $NO{\cdot}H_2O^+$. The negative mode with CF_3O^- has been well documented in the literature[2,3]. In brief, 1 ppmv CF_3OOCF_3 (in N_2) flows through a radioactive ^{210}Po source and CF_3O^- is generated via the following reactions:

$$^{210}\mathrm{Po} \rightarrow \alpha + {}^{206}\mathrm{Pb} \tag{1}$$

$$\alpha + \mathrm{N_2} \rightarrow {\mathrm{N_2}}^+ + \mathrm{e}^- + \alpha \tag{2}$$

$$\mathrm{e}^- + \mathrm{CF_3OOCF_3} \rightarrow \mathrm{CF_3O}^- + \mathrm{CF_3O}\cdot \tag{3}$$

CF_3O^- selectively interacts with multifunctional oxygenated products to generally produce either cluster ion (reaction 4) or fluoride transfer ion (reaction 5):

$$\mathrm{M} + \mathrm{CF_3O} \rightleftharpoons \mathrm{M} \cdot \mathrm{CF_3O}^- \tag{4}$$

$$\mathrm{M} + \mathrm{CF_3O} \rightarrow \mathrm{M\text{-}H}^- \cdot \mathrm{HF} + \mathrm{CF_2O} \tag{5}$$

For the negative mode, the instrument is calibrated for phenol, glycoaldehyde, and H_2O_2, all of which are commercially available. When the authentic standards are not commercially available, we estimate the instrumental sensitivity based on the ion-molecule collision rate coefficients[4,5]. In brief, the conformer-weighted dipole moment and the lowest-energy conformer polarizability of the compound of interest are calculated at the B3LYP/cc-pVTZ level of theory. Next, the dipole moment and polarizability are used to calculate the ion-molecular collision rate coefficients based on an empirical approach[6]. Finally, the ion-molecular collision rate coefficient is related to instrumental sensitivity by using glycoaldehyde as reference compound, the sensitivity of which is experimentally determined. The instrumental sensitivities of major oxidation products are summarized in Table S2.

In the positive mode, $NO{\cdot}H_2O^+$ is produced by flowing 1993±20 ppmv NO (in N_2, Matheson) through the same ^{210}Po source as used in negative mode. The $N_2{}^+$ generated by reaction 2 reacts with NO to form NO^+. Under the trace amount of H_2O in the instrument, the NO^+ is present as $NO \cdot H_2O^+$ and $NO \cdot (H_2O)_2^+$. In contrast to CF_3O^-, $NO \cdot H_2O^+$ is sensitive to less oxygenated compounds, including aromatics, alkanes, and carbonyl species[7–10].

$$N_2{}^+ + NO \rightarrow NO^+ + N_2 \tag{6}$$

$$NO^+ + H_2O \rightleftharpoons NO \cdot H_2O^+ \tag{7}$$

$$M + NO \cdot H_2O^+ \rightleftharpoons M \cdot NO^+ + H_2O \tag{8}$$

The instrumental sensitivity in the positive mode is calibrated for benzene (commercially available), CH_3ONO (synthesized following Taylor et al.[1]), and glyoxal (prepared by following the procedure in Kroll et al.[11]). The sensitivities vary between compounds, but are on the order of $1{\times}10^{-3}$ ncts/ppbv (normalized by the sum of the signal of $NO \cdot H_2O^+$ and $NO \cdot (H_2O)_2^+$) under dry condition (roughly 10 ppmv water vapor in the flow tube). The instrumental sensitivities for other compounds detected in the positive mode are assumed to be the average of that of benzene and glyoxal. For the compounds calibrated here, cluster with NO^+ via reaction 8 is the dominant product ion. This observation is consistent with Guimbaud et al.[12] who measured $C_2H_2O_2{\cdot}NO^+$ as the only product ion for the reaction of glyoxal with NO^+, but inconsistent with Španél et al.[10] who showed that $C_6H_6{\cdot}NO^+$ only accounts for 15% of the benzene + NO^+ products. However, caution is required when applying knowledge on NO^+ ion chemistry to $NO{\cdot}H_2O^+$, because the H_2O molecule can influence the ionization chemistry by carrying away excess energy and minimizing fragmentation. In addition, the instrument configuration and tuning also influence the ion-molecule reaction.

The uncertainty in the instrumental sensitivity is the most important factor hindering

the quantification of product yields. For the compounds without authentic standards, their sensitivities are estimated based on ion-molecule collision rate coefficients in the negative mode and based on the average sensitivity of glyoxal and benzene in the positive mode. We evaluate the uncertainty of the estimated sensitivity by comparing the yields of compounds that are detected in both the positive ($NO{\cdot}H_2O^+$) and negative modes (CF_3O^-). Compounds with chemical formula C_6H_6O, $C_6H_6O_2$, $C_6H_6O_3$, $C_4H_4O_3$, which are of interest to this study, are detected in both modes. The sensitivity of phenol (C_6H_6O) in the negative mode is calibrated based on standard, and the sensitivities of other compounds are estimated as discussed above.

Figure S1 compares the yields of four masses between the negative and positive modes. The C_6H_6O yield agrees within 25% between two modes. For the other three masses, the agreement is generally within 50% for the majority of experiments. For $C_6H_6O_2$, $C_6H_6O_3$, and $C_4H_4O_3$, each mass has multiple isomers, which likely have different sensitivities. This could introducing compensating errors and complicate the comparison. Nonetheless, the reasonable agreement in product yields between positive and negative modes suggests that the estimated sensitivity is on the right order of magnitude and the uncertainty in instrumental sensitivity does not alter the major conclusions of this study, such as the small yields of C6-epoxydicarbonylene.

S3: Yield calculation

The molar yield of a product X is defined as follows

$$Y_X = \frac{\Delta[X]^{\text{corrected}}}{\Delta[\text{benzene}]} = \frac{F \cdot \Delta[X]}{\Delta[\text{benzene}]} \tag{9}$$

where $\Delta[X]$ and $\Delta[X]^{\text{corrected}}$ represent the amount of X formed before and after correction for secondary loss, respectively. $\Delta[\text{benzene}]$ represents the reacted amount of benzene. F is the correction factor for secondary loss of X. The determination of F follows the procedure

Table S2: Instrumental sensitivity and reaction kinetics of major oxidation products in benzene oxidation

Compound	Formula	sensitivity[a] ($\times 10^{-4}$)	k_{OH}[b] ($\times 10^{-11}$)	j[c] ($\times 10^{-5}$)	mode	note
phenol	C_6H_6O	0.94	2.8	N/A	CF_3O^-	d
C-nitrate	$C_6H_7NO_4$	1.6	2.8	N/A	CF_3O^-	e
BCE-nitrate	$C_6H_7NO_5$	1.8	2.8	N/A	CF_3O^-	e
BCP-nitrate	$C_6H_7NO_6$	1.5	2.8	N/A	CF_3O^-	e
2,4-hexadienedial	$C_6H_6O_2$	1.0	7.4	5.4	CF_3O^-	f
C6-epoxydicarbonylene	$C_6H_6O_3$	1.3	7.4	5.4	CF_3O^-	g
fumaraldehydic acid	$C_4H_4O_3$	2.0	3.7	79.2	CF_3O^-	h
epoxy-butandial	$C_4H_4O_3$	2.0	3.0	0.8	CF_3O^-	i
glyoxal	$C_2H_2O_2$	26	1.0	3.9	$NO \cdot H_2O^+$	j
butenedial	$C_4H_4O_2$	24	5.2	79.2	$NO \cdot H_2O^+$	k
benzene	C_6H_6	23	0.12	N/A	$NO \cdot H_2O^+$	l
methyl nitrite	CH_3ONO	12	N/A	110	$NO \cdot H_2O^+$	m

[a] The unit of sensitivity is ncts pptv^{-1} and ncts ppbv^{-1} for negative mode and positive mode, respectively. In the negative mode, the signal is normalized to the sum of the count rates for $^{13}CF_3O^-$ and $^{13}CF_3O^- \cdot H_2O$. In the positive mode, the signal is normalized by the sum of the count rates of $NO \cdot H_2O^+$ and $NO \cdot (H_2O)_2^+$

[b] k_{OH} unit is cm^3 molecule^{-1} s^{-1}. Values at 298 K.

[c] j unit is s^{-1}. Values correspond to light intensity in this study.

[d] Sensitivity is from calibration. k_{OH} is from MCM.

[e] Sensitivity is from theoretical calculation and averaged over all stereo-isomers. k_{OH} is assumed to be the same as phenol.

[f] Sensitivity is from theoretical calculation. k_{OH} and j are for the E,E-$C_6H_6O_2$ isomer from Klotz et al.[13].

[g] Sensitivity is from theoretical calculation. k_{OH} and j are assumed to be same as 2,4-hexadienedial.

[h] Sensitivity is from theoretical calculation. k_{OH} is adapted from Wang et al.[14], which is calculated using traditional transition-state theory. j is assumed to be the same as butenedial.

[i] Sensitivity is assumed to be the same as fumaraldehydic acid. k_{OH} is assumed to be twice the k_{OH} of acetaldehyde. j is assumed to be 0.01 of $j_{butenedial}$.

[j] Sensitivity is from calibration. k_{OH} and j are from MCM.

[k] Sensitivity is assumed to be the average of benzene and glyoxal. k_{OH} and j are for the Z-$C_4H_4O_2$ isomer from Newland et al.[15].

[l] Sensitivity is from calibration. k_{OH} is from MCM.

[m] Sensitivity is from calibration. j is from measurement.

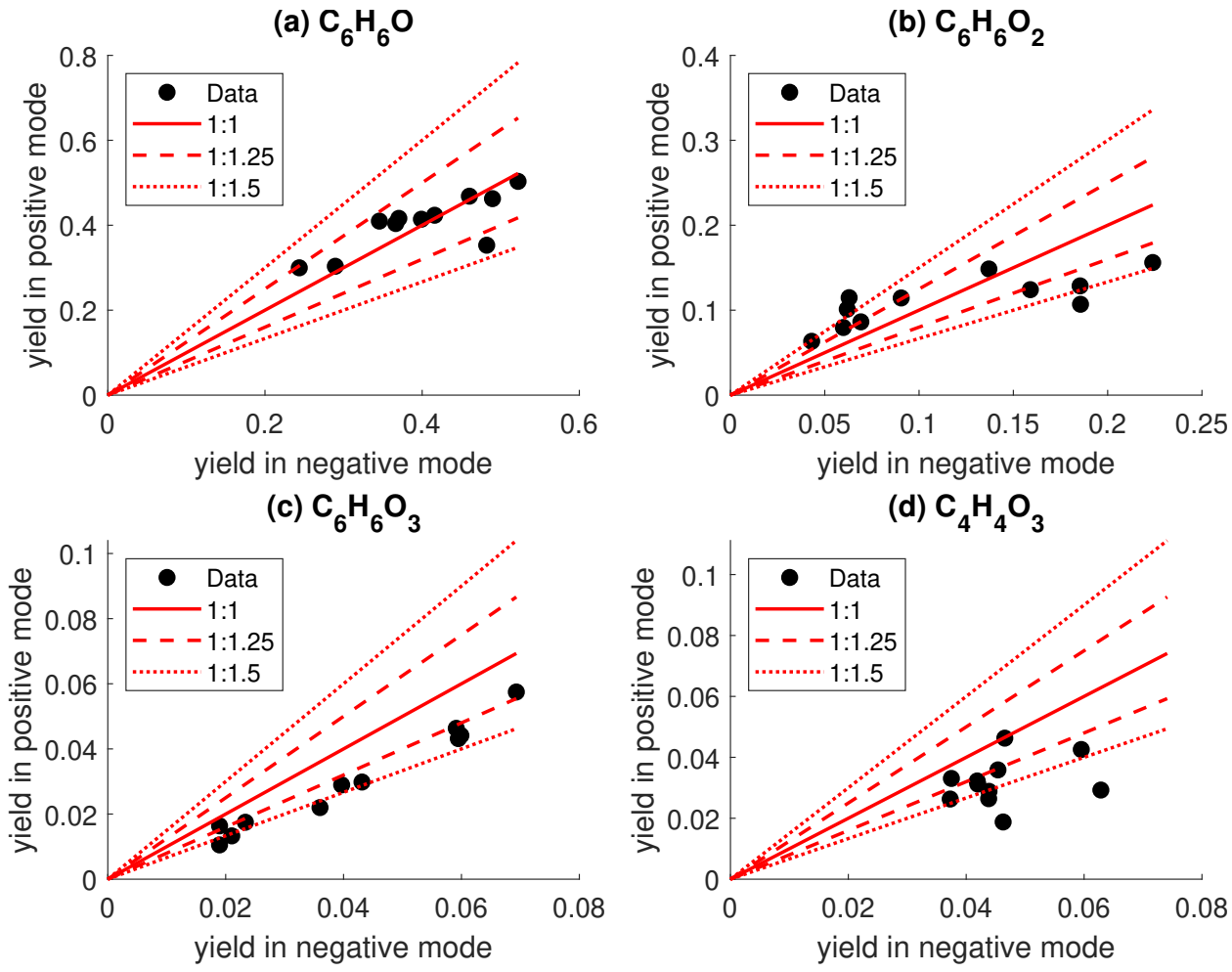

Figure S1: Yield comparison for compounds that are measured in both positive and negative modes.

in Atkinson et al.[16]. In brief, the time-dependent concentrations of benzene and products are governed by

$$\frac{d[\text{benzene}]}{dt} = -k_{\text{benzene+OH}}[\text{benzene}][\text{OH}] \tag{10}$$

$$\begin{aligned}\frac{d[\text{X}]}{dt} &= Y_{\text{X}} \cdot k_{\text{benzene+OH}}[\text{benzene}][\text{OH}] - k_{\text{X+OH}}[\text{X}][\text{OH}] - j_{\text{X}}[\text{X}] \\ &= Y_{\text{X}} \cdot k_{\text{benzene+OH}}[\text{benzene}][\text{OH}] - k_{\text{X,loss}}[\text{X}][\text{OH}]\end{aligned} \tag{11}$$

where $k_{\text{benzene+OH}}$, $k_{\text{X+OH}}$, and j_{X} are the rate coefficients for benzene+OH, X+OH, photolysis of X, respectively. $k_{\text{X,loss}} = k_{\text{X+OH}} + j_{\text{X}}/[\text{OH}]$ represents the effective loss rate of product X, combining its reaction with OH and photolysis. OH concentration in each experiment is determined by fitting the loss rate of benzene. The above two equations can be integrated to obtain

$$F = \left(\frac{k_{\text{benzene+OH}} - k_{\text{X,loss}}}{k_{\text{benzene+OH}}}\right)\left(\frac{1 - \frac{[\text{benzene}]_t}{[\text{benzene}]_0}}{\frac{[\text{benzene}]_t}{[\text{benzene}]_0}^{k_{\text{X,loss}}/k_{\text{benzene+OH}}} - \frac{[\text{benzene}]_t}{[\text{benzene}]_0}}\right) \tag{12}$$

The related reaction kinetics of oxidation products are summarized in Table S2.

In the main text, when comparing the phenol yield between different studies, we correct the phenol production from C-yl + NO_2 reaction, based on Eqn. S13, which is obtained by re-arranging Eqn.3 in the main text. The correction is to facilitate comparison between studies, because both NO and NO_2 concentrations influence the bimolecular lifetime of the radical pool (i.e., C-yl and C-peroxy), but they have different impacts on phenol yield.

$$Y_{\text{phenol}}^{\text{corr,NO}_2} = Y_{\text{phenol}} - \frac{\Phi_{\text{phenol}}\frac{k_6}{K_{\text{eq2}}}\frac{[\text{NO}_2]}{[\text{O}_2]}}{k_{\text{phenol}} + \frac{k_6}{K_{\text{eq2}}}\frac{[\text{NO}_2]}{[\text{O}_2]} + k_{\text{endo,eff}} + k_9\frac{\sum_1^4 K_{\text{eqi}}}{K_{\text{eq2}}}[\text{NO}]} \tag{13}$$

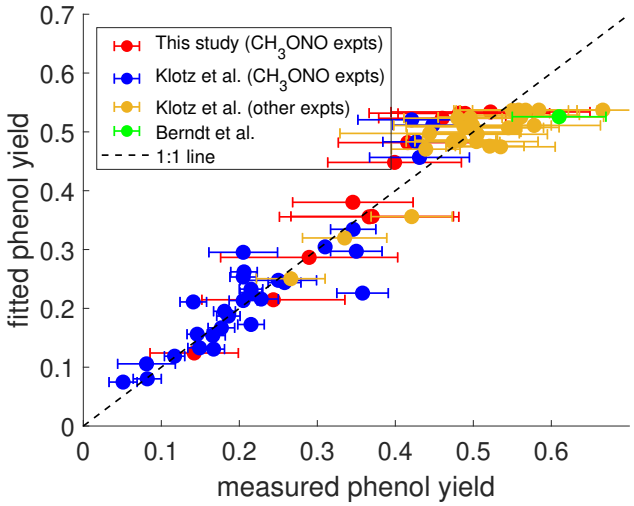

Figure S2: Fitting of phenol yield according to Eqn.3

S4: GC operation and chromtograms

Analytes are sampled from the chamber reactor and cryo-trapped on the head of a 2 m Restek RTX-1701 column at -20°C. After trapping for certain time (5 - 20 min, depending on the analyte concentration), elution is enabled by programmed heating with N_2 as carrier gas. The temperature profile is ramping from -20°C to 50°C at a rate of 20°C min^{-1}; ramping from 50°C to 130°C at a rate of 3°C min^{-1}; held at 130°C for 10 min.

Figures S3 to S8 show the chromatograms and the yields of key oxidation products detected in the negative mode of CIMS. Multiple isomers are resolved for each oxidation product. Regarding $C_6H_7NO_6$ (Figure S5), the 2 m GC column is not efficient in fully separating the two isomer eluting at 1680 s and 1720 s. To separate these two isomers, we represent the two peaks as equal-width Gaussian and fit the chromtograms by employing the peakfit.m function by Dr. Tom O'Haver (https://terpconnect.umd.edu/~toh/spectrum/Introduction.html). Figure S11 shows the output of the algorithm for one representative chromatogram. The GC transmission efficiencies of $C_6H_7NO_6$ and $C_6H_6O_3$ are measured to be 82% and 80%, respectively, by comparing the total chromatogram signal to the amount of analyte trapped in the GC. The GC transmission efficiency would affect the estimated yields of BCP-nitrate and C6-epoxydicarbonylene, because their yields depend on the isomer

separation. The reported yields in the main text are based on the assumption that isomers with the same m/z have the same GC transmission efficiency. To place an upper limit of the yields of BCP-nitrate and C6-epoxydicarbonylene, we assume that they are the only isomers partially lost in the GC and other isomers have 100% GC transmission efficiency. Under this assumption, the yields of BCP-nitrate and C6-epoxydicarbonylene are estimated to be 0.1% and 1.8%, under atmospherically relevant conditions. This does not change the conclusions that the BCP-nitrate yield is unexpectedly low and the C6-epoxydicarbonylene production from BCP-yl is negligible.

To aid the chemical identification of products, we perform H/D exchange analysis and O_3 test. By adding D_2O (D, 99.9%, Cambridge Isotope Laboratories, Inc.) to the GC eluent, the H/D exchange reaction can reveal the number of exchangeable H atoms (-OH, -OOH, and -C(O)OH groups) in the product. The H/D exchange analysis is only performed in the negative mode, not in the positive mode, because high D_2O concentration forms $NO^+ \cdot (D_2O)_n$ clusters. The O_3 test examines the presence of the C-C double bond in the product. After the photooxidation ceases, the oxidation products are evacuated from the chamber and collected in a cold trap at -60°C. Then the trapped analytes are warmed and transferred to a clean chamber using a flow of purified air. 2-4 ppmv O_3 and approximately 90 ppmb cyclohexane (as an OH scavenger) are injected into the chamber. Products with C-C double bond(s) will be quickly consumed by O_3.

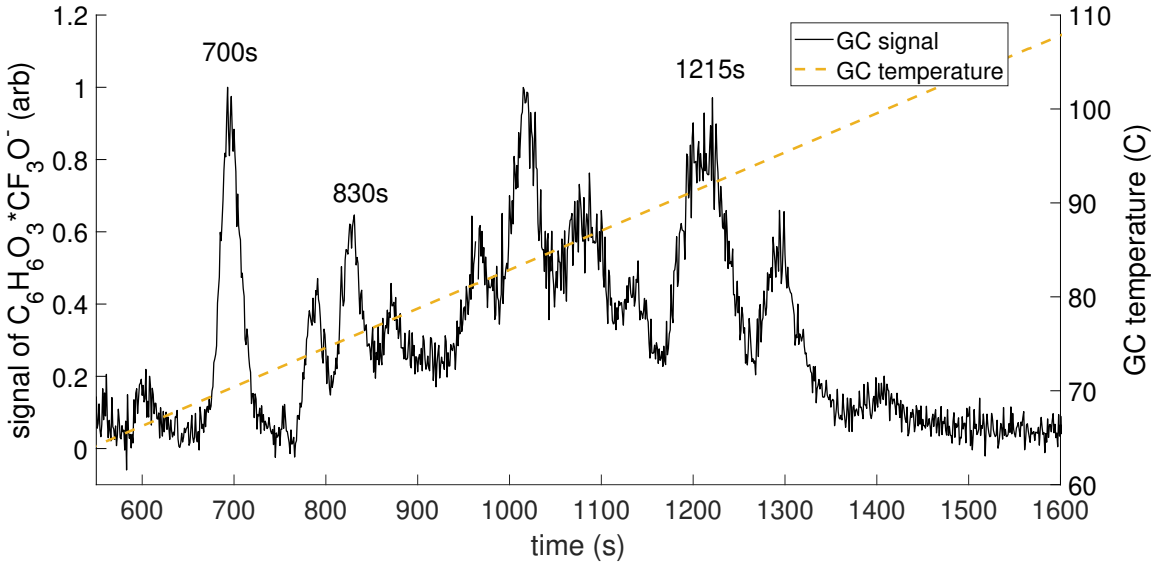

Figure S3: Chromatogram of $C_6H_6O_3 \cdot CF_3O^-$ from an experiment with $\tau_{RO_2,\text{bimolecular}} \approx 0.05$s.

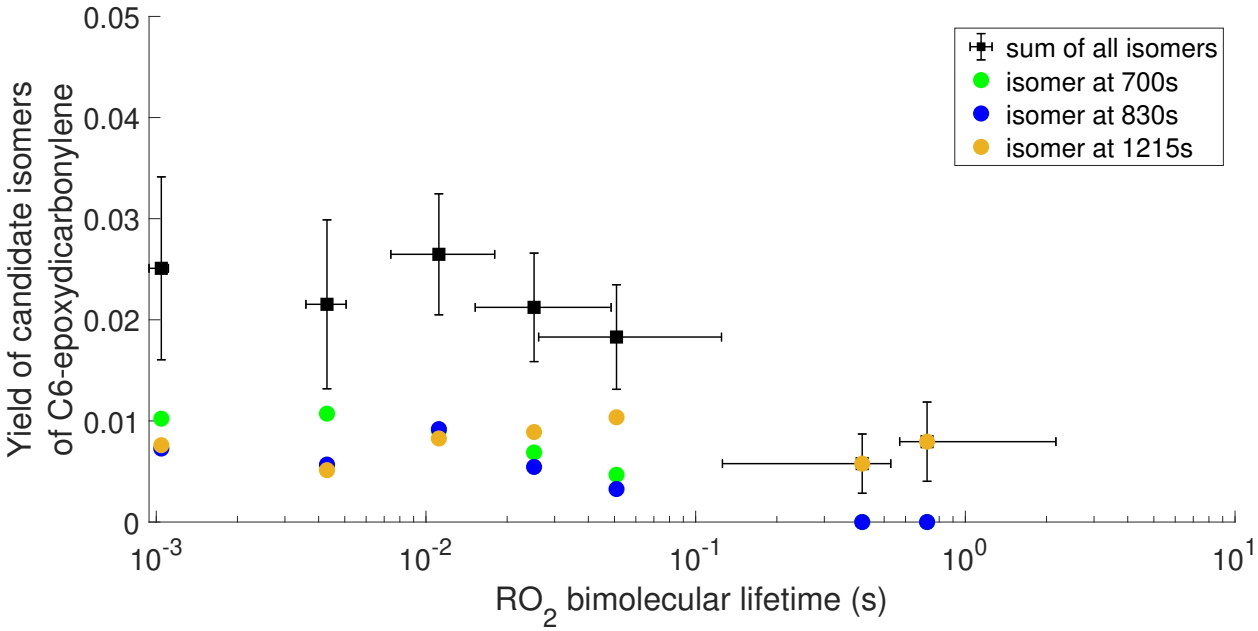

Figure S4: Yield of candidate isomers for C6-epoxydicarbonylene as a function of RO_2 bimolecular lifetime.

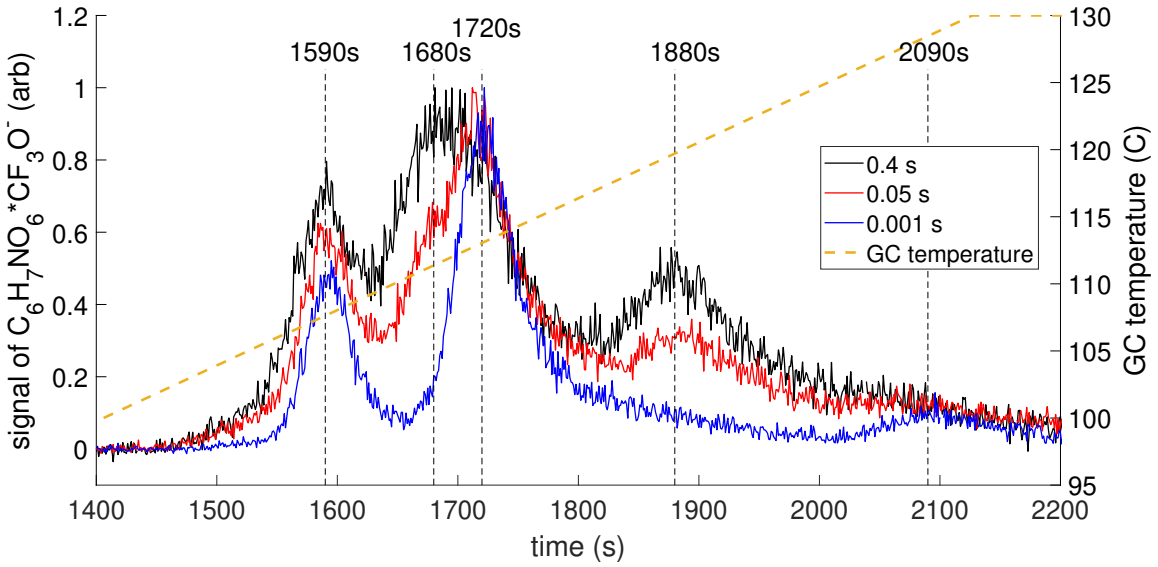

Figure S5: Chromatogram of $C_6H_7NO_6 \cdot CF_3O^-$ from three experiments with different RO_2 bimolecular lifetime. The signals are scaled by the maximum signal of each chromatogram.

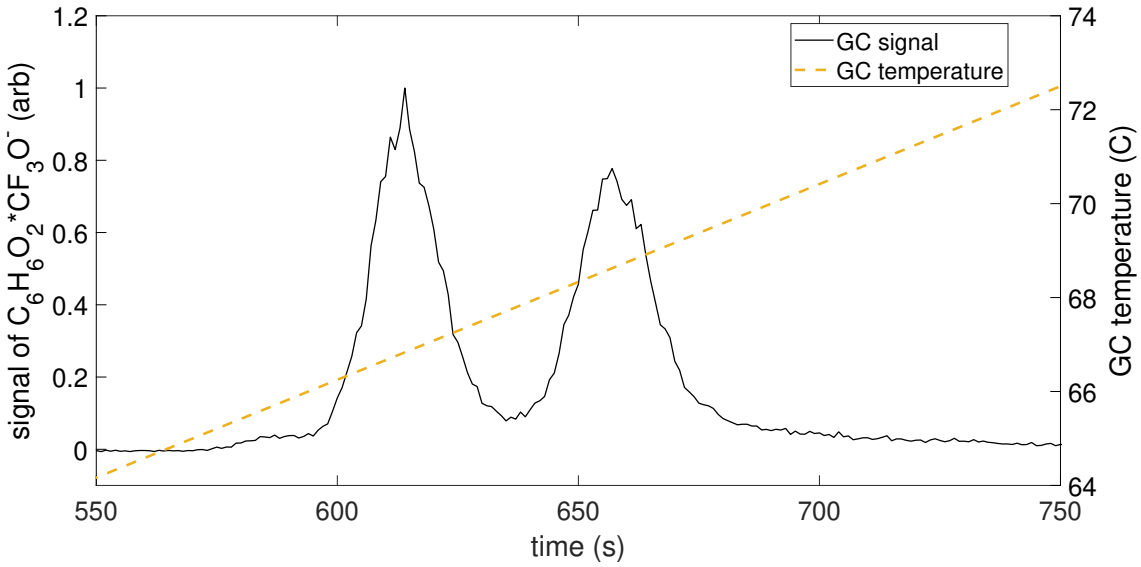

Figure S6: Chromatogram of $C_6H_6O_2 \cdot CF_3O^-$ from an experiment with $\tau_{RO_2,\text{bimolecular}} \approx 0.001$s.

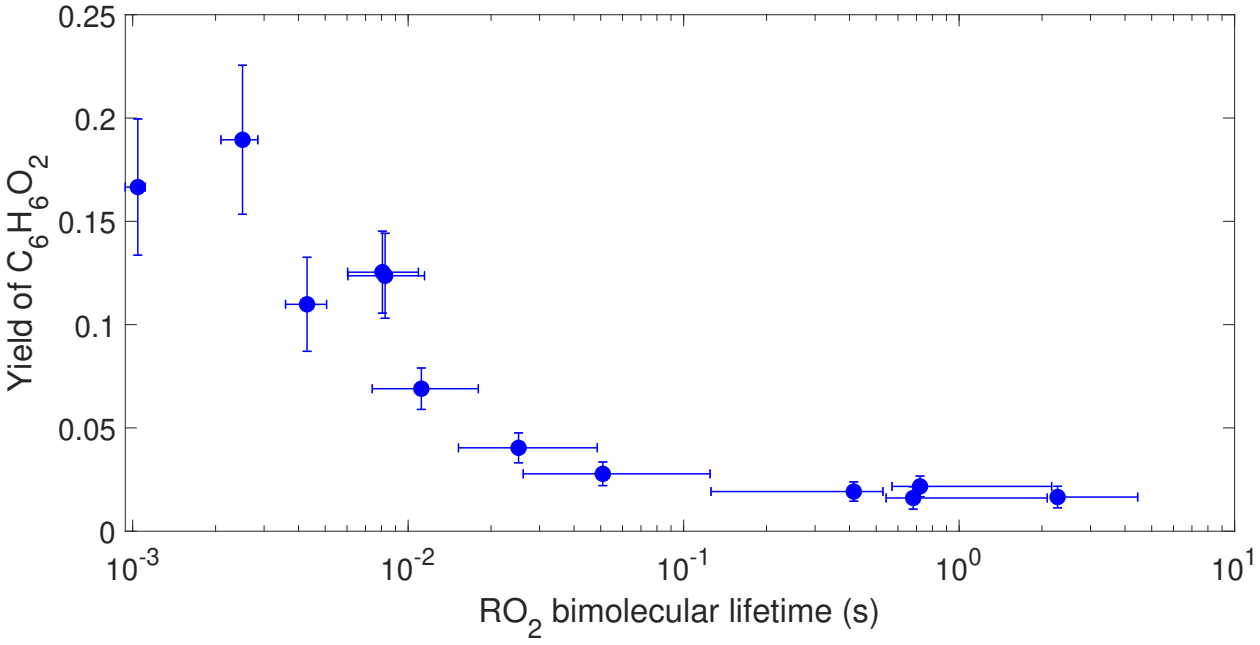

Figure S7: Yield of $C_6H_6O_2$ as a function of RO_2 bimolecular lifetime.

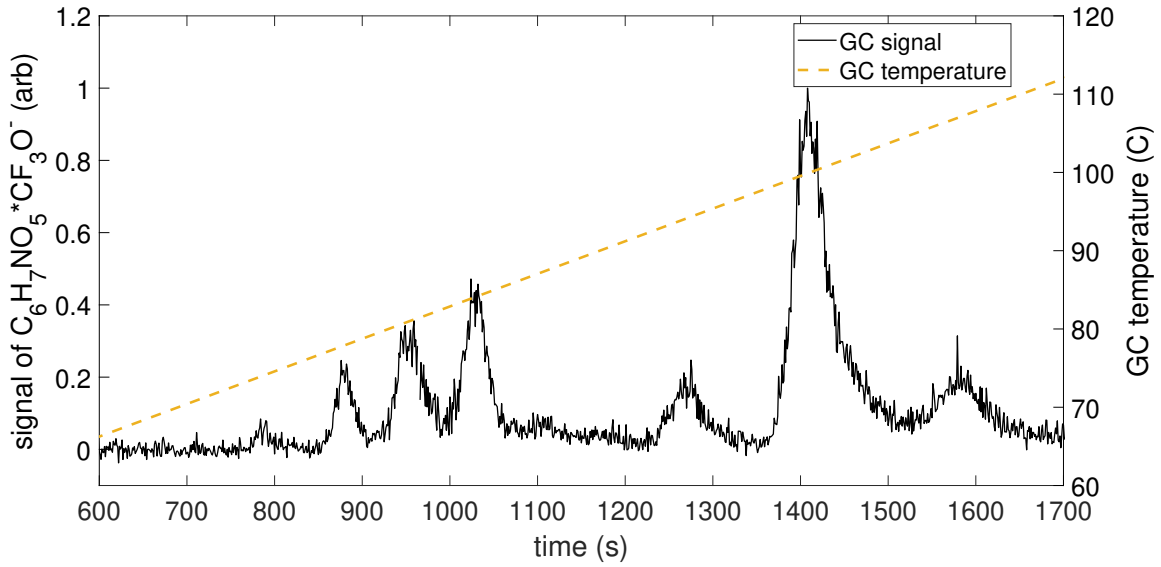

Figure S8: Chromatogram of $C_6H_7NO_5 \cdot CF_3O^-$ from an experiment with $\tau_{RO_2,\text{bimolecular}} \approx 0.05$s.

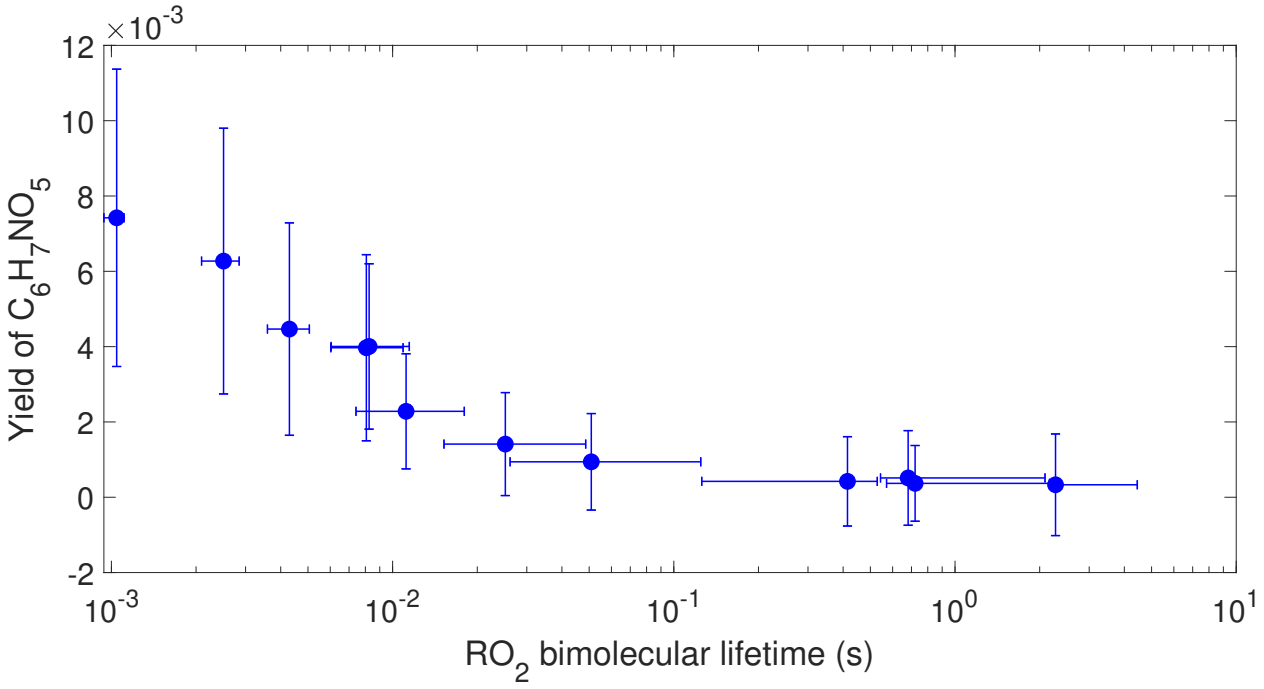

Figure S9: Yield of $C_6H_7NO_5$ as a function of RO_2 bimolecular lifetime.

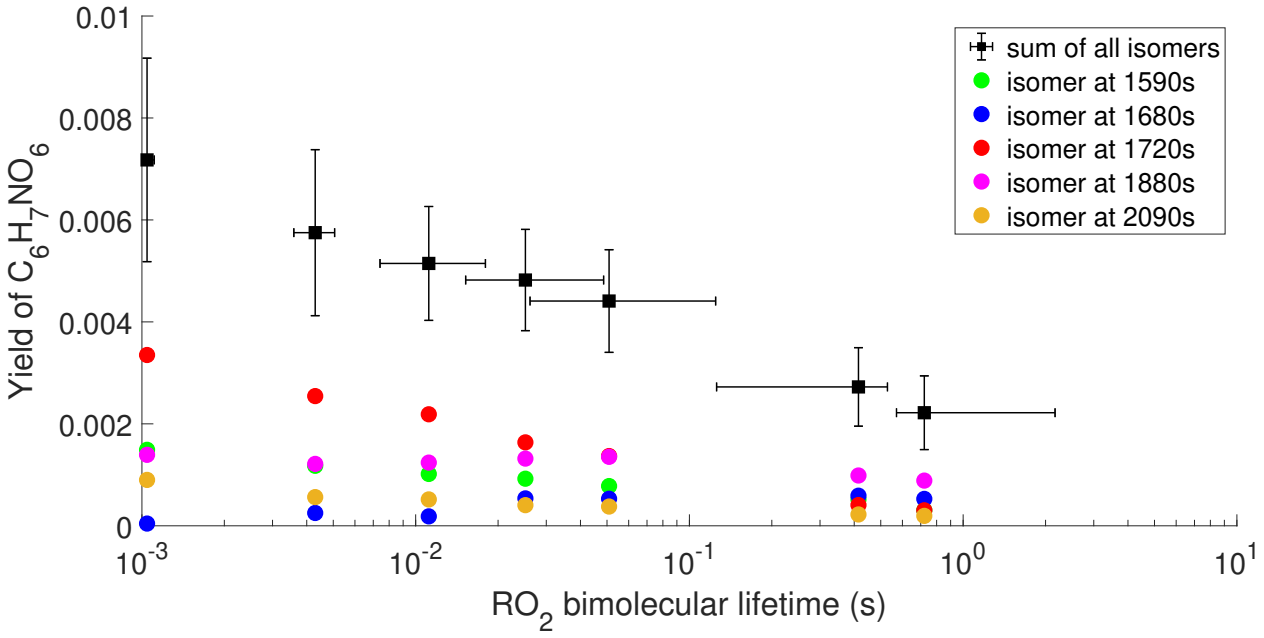

Figure S10: Yield of $C_6H_7NO_6$ as a function of RO_2 bimolecular lifetime.

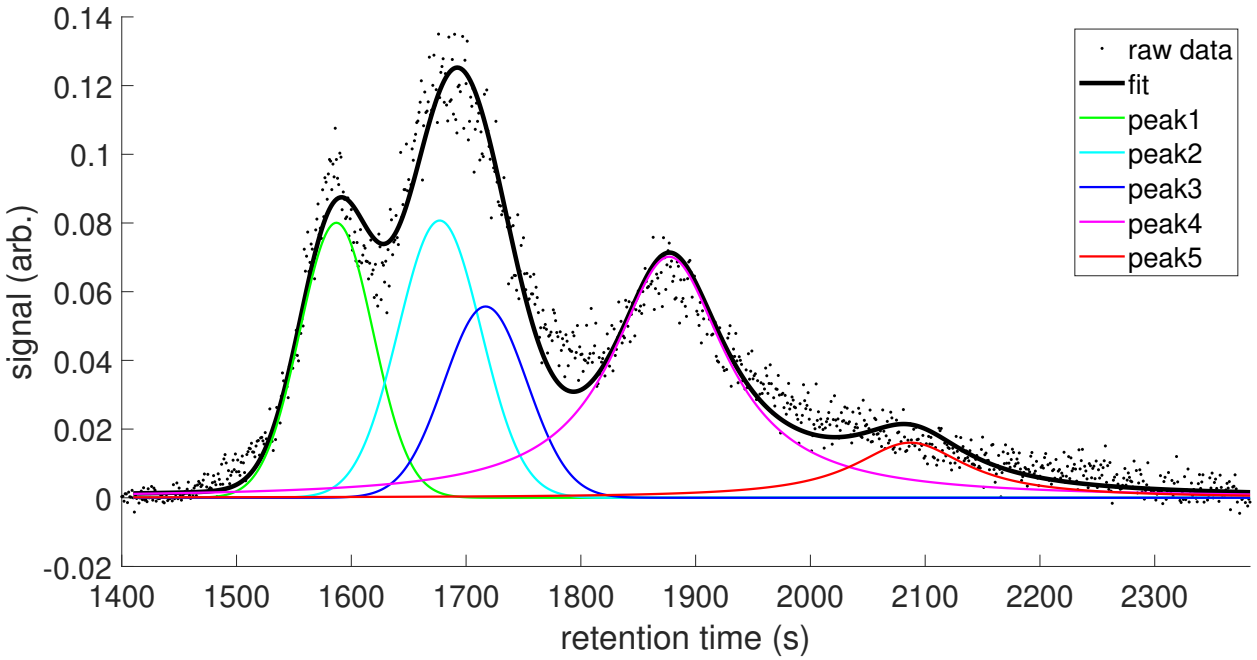

Figure S11: Representative chromatogram of $C_6H_7NO_6 \cdot CF_3O^-$ from an experiment with $\tau_{RO_2,\text{bimolecular}} \approx 0.4$s. The peak shapes of peaks 1-3 and peaks 4-5 are represented by a Gaussian and a Lorentzian, respectively.

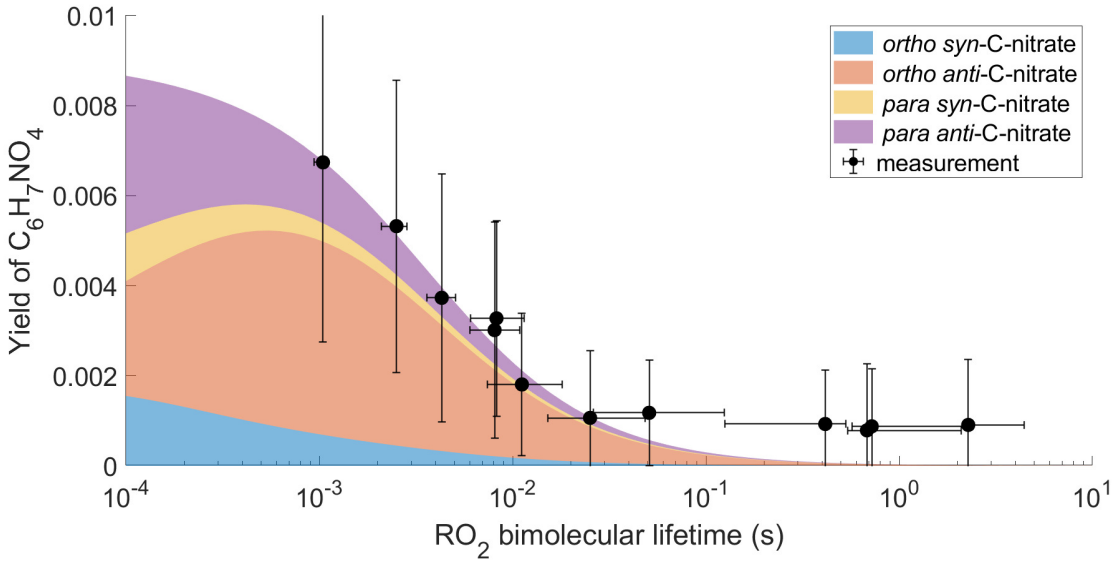

Figure S12: Yield of $C_6H_7NO_4$ as a function of RO_2 bimolecular lifetime ($\tau_{\text{radical,bimolecular}}$). The measured yield represents the sum of all four C-nitrate isomers. The isomer-specific yields are obtained from a kinetic model based on Schemes 1 and 2. The nitrate branching ratio of C-peroxy+NO reaction is optimized to match the measured $\tau_{RO_2,\text{bimolecular}}$-dependent C-nitrate yield. The optimal nitrate branching ratio is 0.9%.

S5: RO_2 bimolecular lifetime

Peroxy radical bimolecular lifetime ($\tau_{RO_2,bimolecular}$) is defined as

$$\tau_{RO_2,bimolecular} = \frac{1}{k_{RO_2+NO}[NO] + k_{RO_2+HO_2}[HO_2]} \quad (14)$$

The values of k_{RO_2+NO} and $k_{RO_2+HO_2}$ are 9.15×10^{-12} and 2.39×10^{-11} cm^3 $molecule^{-1}$ s^{-1}, respectively[17], unless otherwise noted. [NO] and [HO_2] are determined from an updated benzene oxidation mechanism. In the mechanism, the chemistry following a single OH reaction with benzene is based on findings and discussions in the main text. The chemistry of the first-generation closed-shell products is kept the same as that in MCM. However, the model develop and calculation of $\tau_{RO_2,bimolecular}$ are interrelated. On one hand, $\tau_{RO_2,bimolecular}$ is calculated based on model output (i.e., [NO] and [HO_2]). On the other hand, model development requires the radical reaction kinetics, such as k_{phenol}, which are determined based on $\tau_{RO_2,bimolecular}$. Therefore, the determination of radical reaction kinetics and the calculation of $\tau_{RO_2,bimolecular}$ are iterative. We firstly implement theoretically calculated k_{phenol} and $k_{endo,eff}$ into model to obtain initial estimate of $\tau_{RO_2,bimolecular}$. This initial estimate is combined with measured phenol yield to update k_{phenol} and $k_{endo,eff}$. After two iterations, the changes in k_{phenol} and $k_{endo,eff}$ are within 1%. We then obtain the final estimates of $\tau_{RO_2,bimolecular}$, k_{phenol} and $k_{endo,eff}$.

S6: Computational approach

Reaction rate coefficients, k, of selected unimolecular reactions are calculated using multi-conformer transition state theory (MC-TST):[18–21]

$$k = \varkappa \frac{k_B T}{h} \frac{\sum_{i}^{TS\ conf.} \exp\left(\frac{-\Delta E_i}{k_B T}\right) Q_{TS_i}}{\sum_{j}^{R\ conf.} \exp\left(\frac{-\Delta E_j}{k_B T}\right) Q_{R_j}} \exp\left(-\frac{E_{TS} - E_R}{k_B T}\right) \quad (15)$$

$\varkappa$ is the tunneling coefficient calculated using the Eckart approach (see below).[22] k_B is the Boltzmann constant, T is the temperature and h is Planck's constant. The two sums run over the conformers of transition states and reactants, respectively, and sum their partition functions, Q, weighted by their relative zero-point corrected energy, ΔE. The partition functions are evaluated at the lowest-energy vibrational level. The final term depends on the zero-point corrected energy difference between the lowest-energy conformers of TS and reactant, i.e., the reaction barrier.

Conformers, partition functions, and energies are generally calculated as described in Møller et al.[21]. The structure of an arbitrary conformer is optimized using B3LYP/6-31+G(d) in Gaussian 16, rev. C.01.[23–28] Based on this structure, a systematic conformer search is done using MMFF in Spartan'18 with a neutral charge enforced on the radical center.[21,29,30] For the conformer sampling of the transition states, three bond lengths are constrained to their optimized values from the B3LYP/6-31+G(d) optimizations. For peroxy radical H-shifts, these are the O-H bond being formed, the O/C-H bond being broken and the peroxy O-O bond. The conformers from the conformational sampling are optimized at the B3LYP/6-31+G(d) level in Gaussian 16. For the transition states, the TS optimization is preceded by an optimization towards a minimum with the same constraints as used for the conformer search.

Unique conformers within 2 kcal mol^{-1} in electronic energy of the lowest-energy conformer at the B3LYP/6-31+G(d) level are further optimized using ωB97X-D/aug-cc-pVTZ.[21,31–33] For the lowest-energy conformers at this level, an RO-CCSD(T)-F12a/VDZ-F12 (abbreviated F12) single-point calculation is done in Molpro2012.[34–39] The barrier height in the MC-TST equation (Eq. 15) is calculated at the RO-CCSD(T)-F12a/VDZ-F12//ωB97X-D/aug-cc-pVTZ level with ωB97X-D/aug-cc-pVTZ zero-point corrections, while the relative energies between conformers and the partition functions are calculated using omegaB97X-D/aug-cc-pVTZ.

For the tunneling, an IRC is run at the B3LYP/6-31+G(d) level for the TS conformer

lowest in energy at the ωB97X-D/aug-cc-pVTZ level. The end-points are optimized using first B3LYP/6-31+G(d) and subsequently ωB97X-D/aug-cc-pVTZ. Finally, an F12 single-point energy is calculated. The tunneling coefficient is then calculated using the Eckart approach with ωB97X-D/aug-cc-pVTZ imaginary frequency and F12//ωB97X-D/aug-cc-pVTZ Eckart barriers with ωB97X-D/aug-cc-pVTZ zero-point corrections. All rate coefficients are calculated at 298.15 K and are high-pressure limit values.

For the alkoxy radicals, no F12 calculations are done due to potential issues with the HF reference wave function[40] and instead, the ωB97X-D values are used. For the ωB97X-D of the reactions of the BCP-oxy radical, the 6-311+G(d,p) basis set is used instead of the aug-cc-pVTZ basis set as no TS could be located for the 1,5 aldehydic H-shift with the aug-cc-pVTZ basis set.

S7: Unimolecular reactions of C-peroxy

We calculate the unimolecular reaction rate coefficients of C-peroxy isomers using MC-TST. Calculation results at the B3LYP/6-31+G(d) level, summarized in Scheme S1, show that the endo-cyclization and HO_2 elimination are the dominant reactions for *ortho-syn*-C-peroxy and *ortho-anti*-C-peroxy, respectively. These two reaction pathways are re-evaluated at the F12 level. The rate coefficients of all studied unimolecular reactions of *para*-C-peroxy are below 3×10^{-5} s^{-1} at the B3LYP/6-31+G(d) level, suggesting these unimolecular reactions are negligible under atmospheric conditions.

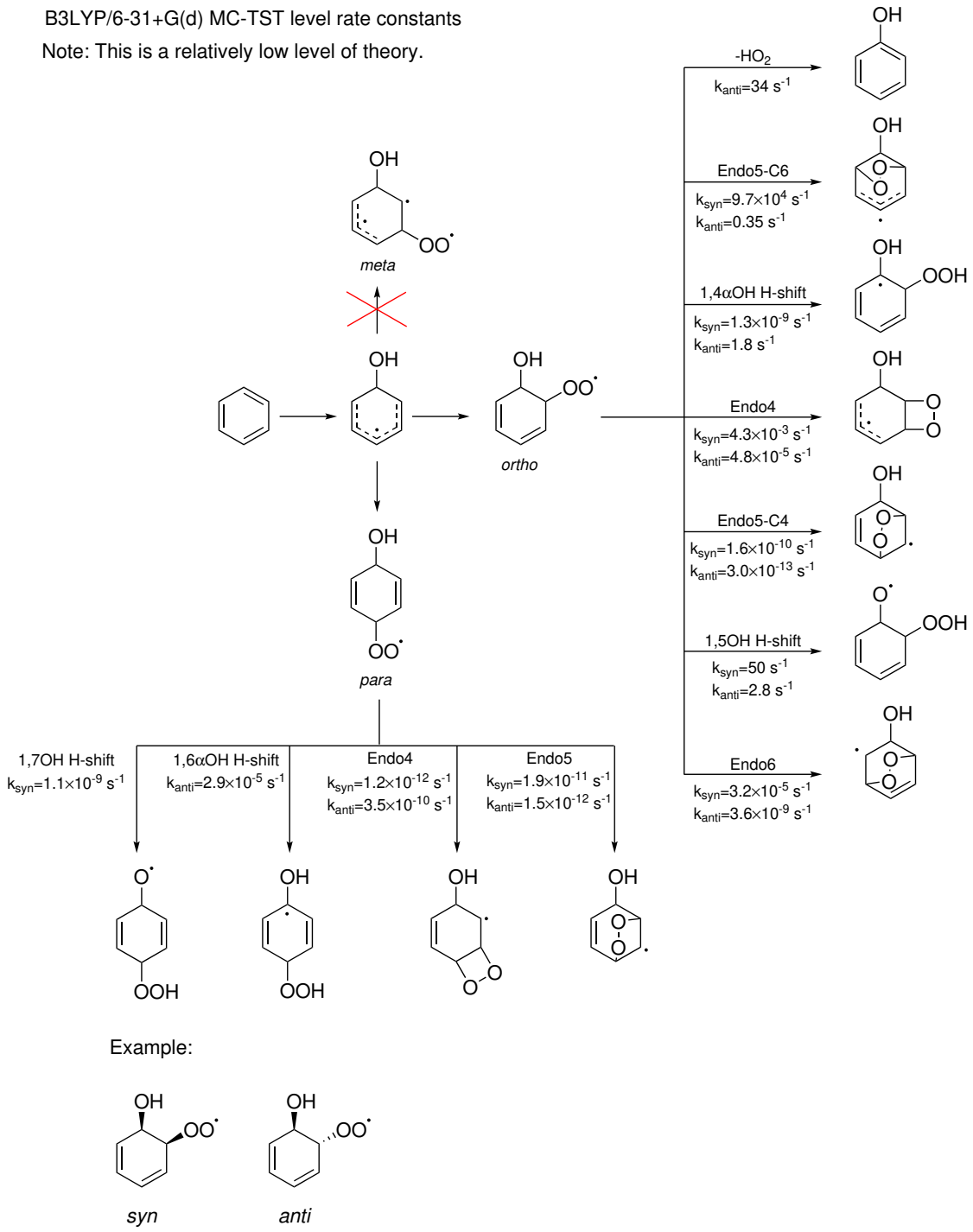

Scheme S1: Calculated unimolecular reaction rate coefficient for C-peroxy isomers at the B3LYP/6-31+G(d) MC-TST level. The HO_2 elimination rate of *ortho-anti*-C-peroxy is calculated at the at the ωB97X-D/6-31+G(d) level.

Table S3: Calculated unimolecular reaction rate coefficients of C-peroxy. All values are calculated at 298 K, except for this study at 298.15 K.

reaction	rate coefficient (s^{-1})	reference[a]	note
ortho-syn-C-peroxy → BCP-yl	2.5×10^{5}	Raoult et al.[41]	b
	3.07×10^{3}	Glowacki et al.[42]	c
	3.6×10^{2}	Olivella et al.[43]	d
	8.1×10^{2}	this study	e
ortho-anti-C-peroxy → phenol	4.3×10^{1}	Glowacki et al.[42]	f
	1.3×10^{2}	this study	e

[a] Lay et al.[44] also calculated the unimolecular reactions of C-peroxy, but are not included in this table because of the relatively low level of theory used in that study.
[b] TST, B3LYP/6-31G(d) with the activation enthalpy corrected by the empirical "Intrinsic-Method" (IM).
[c] Bartis-Widom Eigenvalue-Eigenvector Analysis, 760 Torr, barriers calculated using CASPT2 on PES adjusted within expected uncertainties to best fit experimentally observed decay of C-yl (Benzene-OH)
[d] TST, ROCCSD(T)/6-311+G(2df,2p)// B3LYP/6-31G(d).
[e] MC-TST, RO-CCSD(T)-F12a/VDZ-F12//ωB97X-D/aug-cc-pVTZ.
[f] Bartis-Widom Eigenvalue-Eigenvector Analysis, 760 Torr, barriers calculated using G3X(MP2)-RAD but adjusted within its estimated uncertainty limit ($\sim$ 5 kJ mol^{-1}) to best fit experimentally observed decay of C-yl (Benzene-OH)

Table S4: Kinetic parameters adopted from the literature and used in Eqn.3

Parameter	Value	Unit	Reference
Φ_{phenol,NO_2}	5.9	%	Klotz et al.[45]
k_1	2.8×10^{-15}	cm^3 $molecule^{-1}$ s^{-1}	Glowacki et al.[42]
k_{-1}	9.8×10^{4}	s^{-1}	Glowacki et al.[42]
k_2	8.4×10^{-16}	cm^3 $molecule^{-1}$ s^{-1}	Glowacki et al.[42]
k_{-2}	2.8×10^{3}	s^{-1}	Glowacki et al.[42]
k_3	4.2×10^{-14}	cm^3 $molecule^{-1}$ s^{-1}	Glowacki et al.[42]
k_{-3}	2.6×10^{6}	s^{-1}	Glowacki et al.[42]
k_4	2.6×10^{-14}	cm^3 $molecule^{-1}$ s^{-1}	Glowacki et al.[42]
k_{-4}	4.8×10^{5}	s^{-1}	Glowacki et al.[42]
k_6	2.8×10^{-11}	cm^3 $molecule^{-1}$ s^{-1}	Knispel et al.[46]
k_9	1.7×10^{-11}	cm^3 $molecule^{-1}$ s^{-1}	Klotz et al.[45]

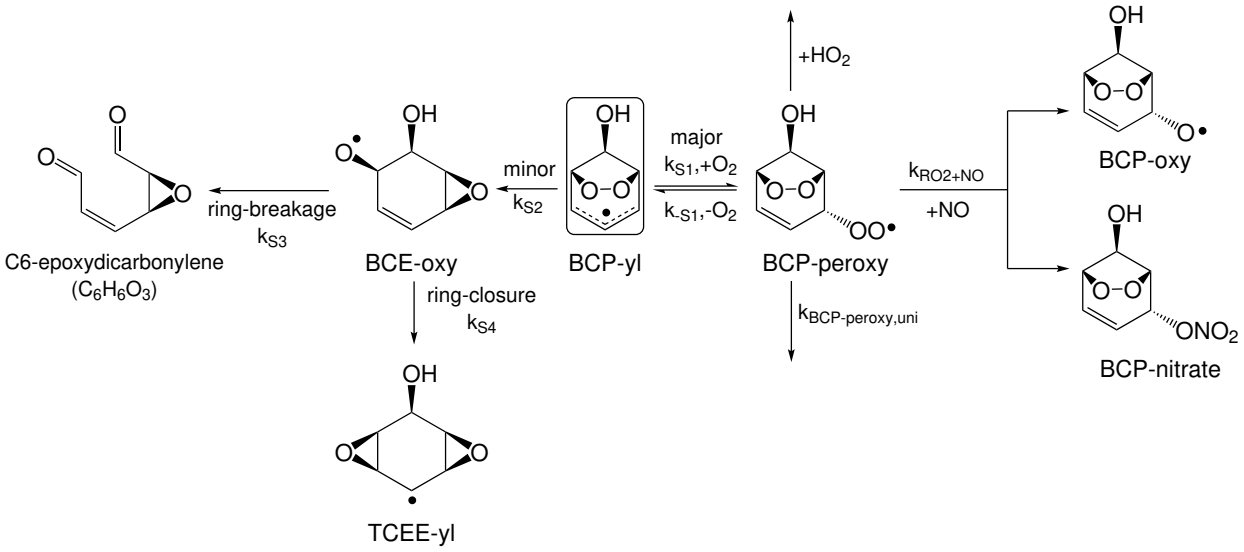

Scheme S2: Reaction scheme of BCP-yl.

S8: Loss rate of BCP-yl

This section compares the effective loss rate of BCP-yl by O_2 addition (denoted as $k_{eff,BCP\text{-}peroxy}$) and by isomerization channel (k_{S2}). By considering the reversible O_2 addition to BCP-yl and assuming reaction with NO as the sole fate of BCP-peroxy (Scheme S2),

$$k_{eff,BCP-peroxy} = k_{RO_2+NO}[NO]\frac{k_{S1}[O_2]}{k_{-S1}} = k_{RO_2+NO}K_{eq,S1}[NO][O_2] \quad (16)$$

where k_{RO_2+NO} = 9.15×10^{-12} cm^3 s^{-1} molecule^{-1}. The equilibrium constant ($K_{eq,S1} = k_{S1}/k_{-S1}$) is uncertain. We estimate its value by using three different approaches. First, the calculated $K_{eq,S1}$ is 2.4×10^{-17} at ωB97X-D/aug-cc-pVTZ level of theory. Second, the calculated $K_{eq,S1}$ is 5.9×10^{-15}cm^{3}molecule^{-1} at RO-CCSD(T)-F12a/VDZ-F12// ωB97X-D/aug-cc-pVTZ level of theory. Third, by analogizing to equilibrium between BCP-yl and BCP-peroxy to that of isoprene system, $K_{eq,S1}$ is on the order of 10^{-13}cm^{3}molecule^{-1} (i.e., $2 \times 10^{-12}/20$ from Teng et al.[47]). By applying the estimated range of $K_{eq,S1}$ and assuming 1 ppbv NO and atmospheric O_2 concentration, $k_{eff,BCP\text{-}peroxy}$ is calculated to range from 30 to 10^5 s^{-1}. We also theoretically calculate the isomerization rate of stabilized BCP-yl (k_{S2}) to be 0.02 s^{-1}. Thus, regardless of the uncertainty, $k_{eff,BCP\text{-}peroxy}$ is orders of magnitude

faster than the k_{S2}.

S9: Unimolecular reactions of BCP-peroxy

Two unimolecular reactions have been theoretically investigated as shown in Scheme S3.

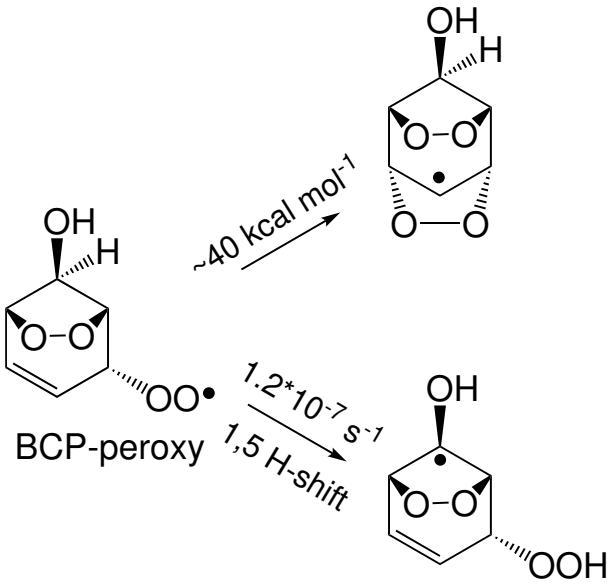

Scheme S3: Explored unimolecular reactions of BCP-peroxy. The rate coefficient of H-shift is calculated using the MC-TST approach by Møller et al.[21] with barriers at the F12 level. The barrier height of endo-cyclization is calculated by Motta et al.[48].

S10: BCP-oxy chemistry

Uncertainties in theoretical calculation of BCP-oxy reaction

Wang et al.[49] calculated the branching ratio of BCP-oxy chemistry and suggested ring-closure to be preferential. However, new calculation results from the same group suggest less than 2% of BCP-oxy undergoes ring-closure (Figure 1 in Wang et al.[14]). The theoretical calculation is highly uncertain because of the reversibility of BCP-oxy ring-closure reaction and the unknown O_2 addition rate to TCPE-yl (Scheme S4).

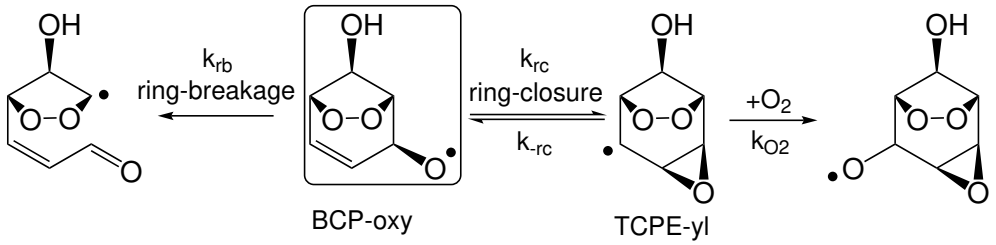

Scheme S4: Reaction pathways of *syn*-BCP-oxy.

The effective removal rate of BCP-oxy by ring-closure ($k_{eff,rc}$) can be represented as

$$k_{eff,rc} = \frac{k_{O_2}[O_2]k_{rc}}{k_{-rc} + k_{O_2}[O_2]} \tag{17}$$

where k_{O_2} represents the O_2 addition rate coefficient to TCPE-yl. k_{rc} and k_{-rc} represent the forward and reverse rate coefficients of ring-closure of BCP-oxy, which are calculated to be 2.84×10^9 and 3.97×10^9 s^{-1}, respectively, by Wang et al.[49]. $[O_2]$ represents the atmospheric O_2 concentration. Using a value of $6 \times 10^{-12}cm^3molecule^{-1}s^{-1}$ for k_{O_2}, $k_{eff,rc}$ is calculated to be equal to the ring-breakage rate coefficient of BCP-oxy (i.e., $k_{rb} = 2.2 \times 10^7$ s^{-1}). This leads to the ratio of ring-closure to ring-breakage to be 1, which is the predicted value in Wang et al.[49]. However, k_{O_2} is poorly constrained. If k_{O_2} was 1×10^{-12} cm^3 $molecule^{-1}$ s^{-1}, the ratio of ring-closure to ring-breakage would decrease to 0.17. Therefore, the theoretically predicted fate of BCP-oxy is highly sensitive to the O_2 addition rate coefficient.

The fate of BCP-oxy is expected to be stereospecific. Wang et al.[49] only studied the *syn* isomer, because this isomer is proposed to be produced from the isomerization of *syn*-BCP-peroxy and the stereo-structure is inherited. The reactions of other stereoisomers generated from C-oxy channel require further investigation.

Uncertainties in experimental estimate of BCP-oxy fate

To experimentally investigate the fate of BCP-oxy, we use the measurement of epoxybutandial, a unique product from BCP-oxy ring-closure pathway. This constraint is only

applicable under low NO conditions (i.e., NO $<$ a few ppbv) when BCP-oxy is the dominant source of epoxy-butandial. Under high NO conditions when C-peroxy+NO is substantial, epoxy-butandial can also be produced from TCEE-yl (Scheme S10). Another to note is taht epoxy-butandial and fumaraldehydic acid are structural isomers with the same chemical formula $C_4H_4O_3$. Their separation based on gas chromatography will be discussed in next section.

One uncertainty in using epoxy-butandial yield to constrain the BCP-oxy fate is the unstudied photochemical reaction rates of epoxy-butandial. We assume that the k_{OH} of epoxy-butandial is twice the k_{OH} of acetaldehyde, as epoxy-butandial has two aldehyde functionality. We assume $j_{epoxy-butandial} = 0.01 \times j_{butenedial}$ because Newland et al.[15] noted that the photolysis rate of unsaturated aldehyde is roughly 100 times larger than that of saturated aldehyde. Even assuming that epoxy-butandial has the same fast secondary loss as butenedial, the epoxy-butandial yield only increases from 0.2% to 0.3%. The instrumental sensitivity of epoxy-butandial also influences the estimate of BCP-oxy fate. However, even if we assume the instrumental sensitivity of epoxy-butandial is 10 times of current assumption, the epoxy-butandial yield increases from 0.2% to 2%, suggesting only 4% of BCP-oxy undergoing ring-closure. In conclusion, these uncertainties unlikely alter the conclusion that ring-closure is a minor reaction of BCP-oxy and ring-breakage is its dominant fate.

Separation of epoxy-butandial and fumaraldehydic acid

Epoxy-butandial and fumaraldehydic acid are structural isomers with the same chemical formula $C_4H_4O_3$. They are separated based on gas chromatography and their different ion-chemistry with CF_3O^-. It is expected that epoxy-butandial reacts with CF_3O^- mainly via clustering chemistry ($C_4H_4O_3 \cdot CF_3O^-$ at m/z 185), while fumaraldehydic acid could potentially react both by clustering ($C_4H_4O_3 \cdot CF_3O^-$ at m/z 185) and fluoride transfer ($C_4H_4O_3 \cdot F^-$ at m/z 119). The chromtograms of $C_4H_4O_3 \cdot CF_3O^-$ and $C_4H_4O_3 \cdot F-$ have two peaks each. We infer both $C_4H_4O_3 \cdot F^-$ peaks represent fumaraldehydic acid and $C_4H_4O_3 \cdot$

CF_3O^- peak eluting at 720s represents epoxy-butandial based on the following analysis. First, the H/D exchange analysis reveals that the $C_4H_4O_3 \cdot CF_3O^-$ peak eluting at 720s does not contain any exchangeable acidic H, consistent with the structure of epoxy-butandial. Both $C_4H_4O_3 \cdot F^-$ peaks have one acidic H, consistent with the structure of fumaraldehydic acid. Second, in benzene-d_6 oxidation experiments, two $C_4D_3HO_3 \cdot F^-$ peaks (i.e., replacing three hydrogen atoms in $C_4H_4O_3 \cdot F^-$ with deuterium atoms) are observed, which is consistent with their proposed formation mechanism (Scheme S5). However, we note that the two peaks of $C_4H_4O_3 \cdot F–$ unlikely arise from the same molecule, because they exhibit different ion-chemistry with CF_3O^-. The molecule eluting at 720s reacts with CF_3O^- via only fluoride transfer, while the molecule eluting at 1000s undergoes both fluoride transfer and clustering reactions with CF_3O^- (i.e., both $C_4H_4O_3 \cdot CF_3O^-$ and $C_4H_4O_3 \cdot F^-$ have a peak eluting at 1000s). Without authentic standard, the further peak assignment is challenging. We assume both peaks represent fumaraldehydic acid and use the summed signal to obtain an upper bound of fumaraldehydic acid yield. Authentic standard of fumaraldehydic acid will be critical to improve its quantification and hence constrain the fate of BCP-oxy.

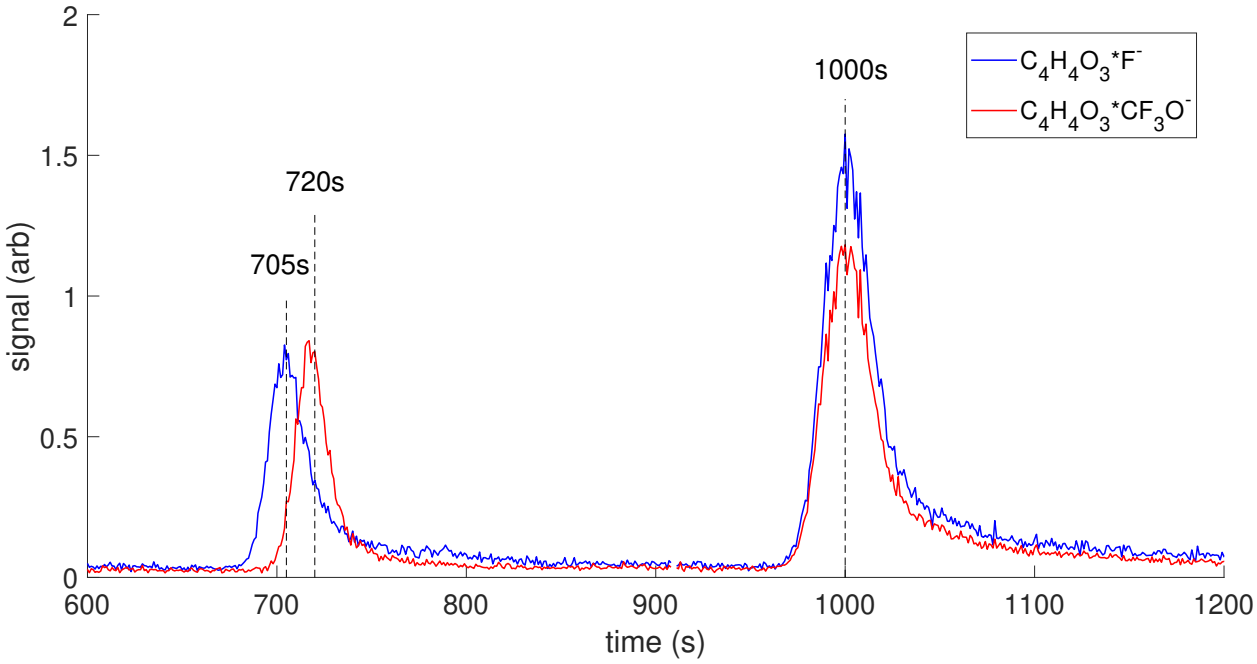

Figure S13: Chromatograms of $C_4H_4O_3 \cdot CF_3O^-$ and $C_4H_4O_3$ fluoride transfer product from an experiment with $\tau_{RO_2,\text{bimolecular}} \approx 0.001$s.

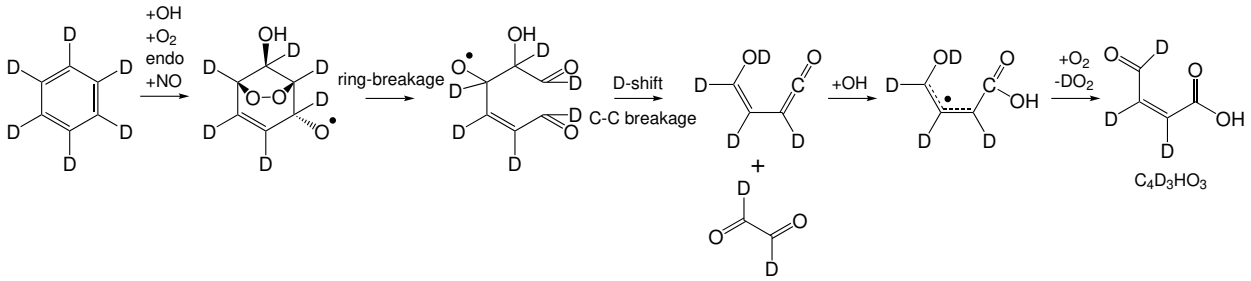

Scheme S5: Formation of $C_4D_3HO_3$ from the oxidation of d6-benzene.

Theoretical study of BCP-oxy, $C_6H_7O_4$-oxy and $C_6H_7O_4$-yl reactions

In this section, we discuss our theoretical study of the BCP-oxy, $C_6H_7O_4$-oxy, and $C_6H_7O_4$-yl reactions. C-C bond scission is the initial step in the conversion of BCP-oxy to $C_6H_7O_4$-oxy. Intrinsic Reaction Coordinate (IRC) calculations for this reaction at the ωB97X-D/6-31+G(d) level lead to a structure in which the newly formed aldehyde group is perpendicular to the double bond. This suggests that the $C_6H_7O_4$-oxy radical will be formed as both *cis* and *trans* isomers with respect to the central bond in the conjugated aldehyde group (Scheme S6) which have ωB97X-D/6-311+G(d,p) zero-point corrected energies within 0.05 kcal mol^{-1} of each other. The ωB97X-D/6-311+G(d,p) barrier for the interconversion between these is about 5 kcal mol^{-1}. This barrier is higher than the barriers for some of the other unimolecular reaction pathways available (Table S5) and therefore these two isomers may react independently. Decomposition is calculated to be the dominant pathway for *cis*-$C_6H_7O_4$-oxy, yielding gloyxal and butenedial. In contrast, for *trans*-$C_6H_7O_4$-oxy, the 1,5-aldehydic H-shift leading to $C_6H_7O_4$-yl is also expected to be an important pathway, as the barrier is ∼3 kcal mol^{-1} lower than that for the decomposition (Table S5). The isomer-specific chemistry of $C_6H_7O_4$-oxy is not specifically discussed by Wang et al.[14].

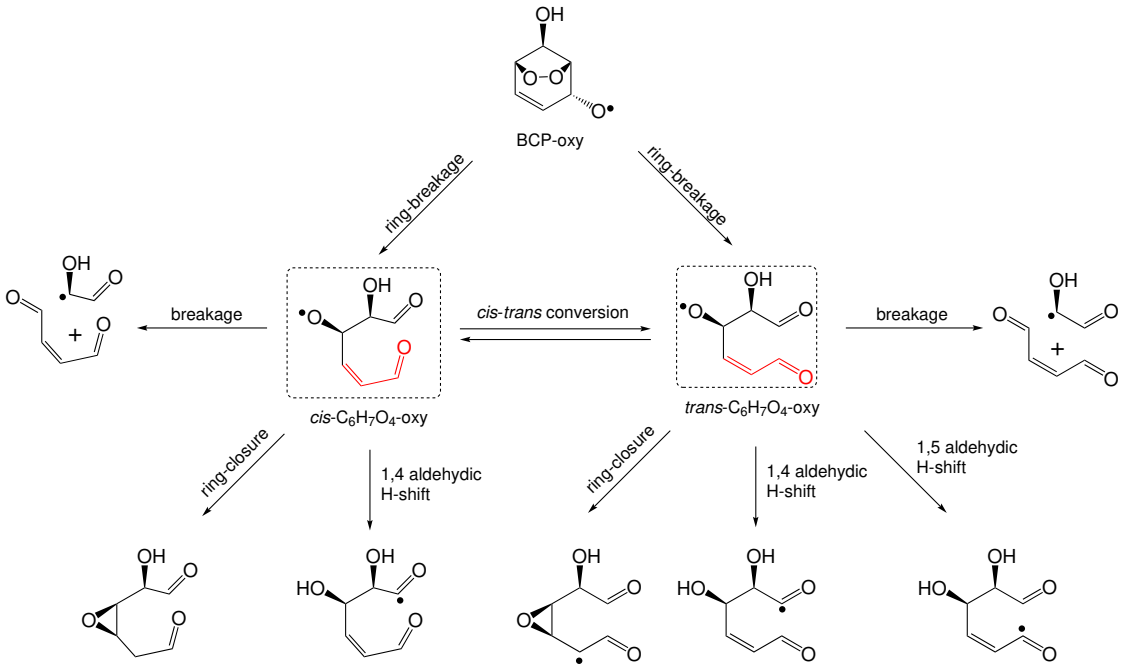

Scheme S6: Overview of BCP-oxy ring-breakage leading to *cis* and *trans*-$C_6H_7O_4$-oxy and their unimolecular reactions.

Table S5: ωB97X-D/6-311+G(d,p) zero-point corrected barrier heights (in kcal mol^{-1}) for the unimolecular reactions of the *cis* and *trans*-$C_6H_7O_4$-oxy radicals shown in Scheme S6.

Reaction	ΔE_{cis}	ΔE_{trans}
Cis-trans-conversion	5.1	5.1
1,4 aldehydic H-shift	7.5	10.7
1,5 aldehydic H-shift	N/A	-0.3
Ring-breakage	1.5	2.8
Ring-closure	7.1	5.7

The 1,5-aldehydic H-shift of *trans*-$C_6H_7O_4$-oxy produces an alkyl radical $C_6H_7O_4$-yl (R3 and R6 in Scheme S7). Wang et al.[14] suggested that the $C_6H_7O_4$-yl exclusively decomposes into a ketene-enol accompanied by gloyxal (R11 in Scheme S7), rather than reacting with O_2. In agreement with Wang et al.[14], we find that the $C_6H_7O_4$-yl radical is about 70 kcal mol^{-1} lower in energy than BCP-oxy and thus is unlikely to react with O_2 before undergoing unimolecular reactions via the excess energy. However, given the amount of excess energy and multiple substituents in the $C_6H_7O_4$-yl, the decomposition is not the only possible unimolecular reaction of $C_6H_7O_4$-yl.

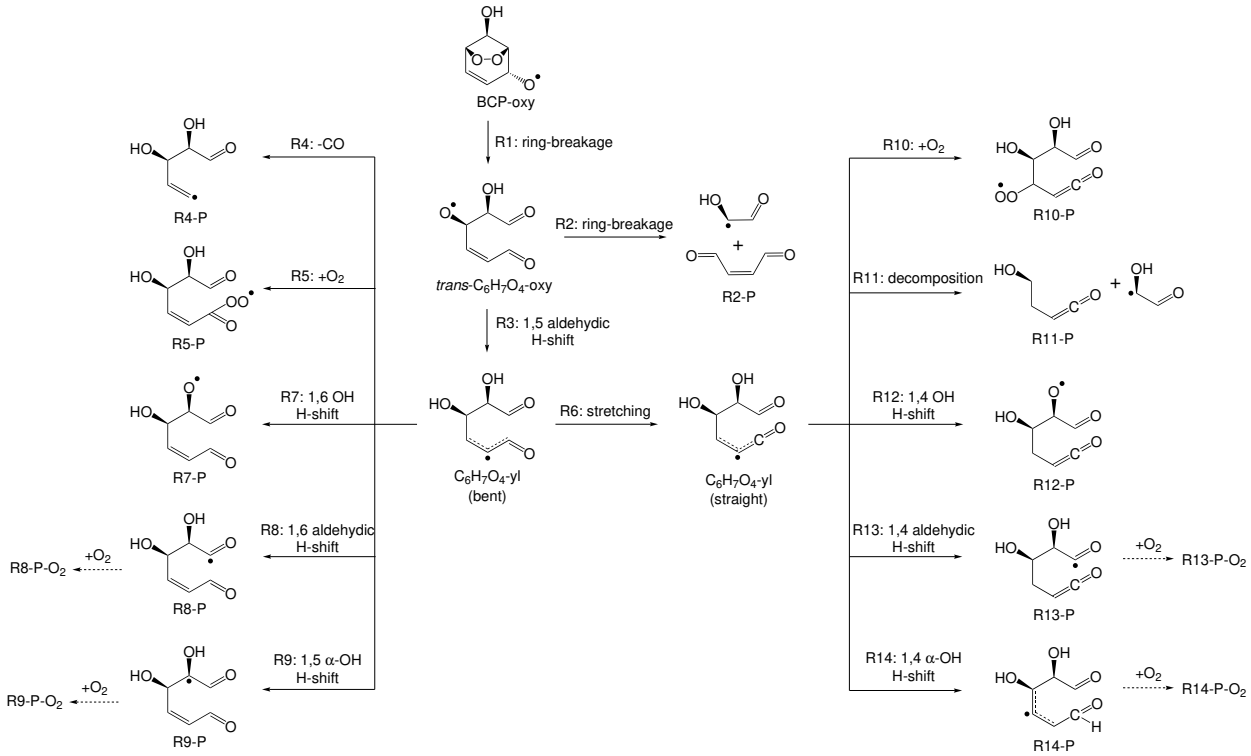

Scheme S7: Overview of studied unimolecular reactions for the $C_6H_7O_4$-yl radical formed from the 1,5 aldehydic alkoxy H-shift of the *trans*-$C_6H_7O_4$-oxy radical. An IRC calculation shows that the 1,4 α-OH H-shift (R14) is connected to $C_6H_7O_4$-yl (straight) rather than the bent isomer. The relative energies of the species and transition states are given in Table S6. The ring-breakge of BCP-oxy (R1) can also produce *cis*-$C_6H_7O_4$-oxy radical, which is not included in the RRKM-ME modeling.

Table S6: ωB97X-D/6-311+G(d,p) zero-point corrected energy (in kcal mol^{-1}) of transition states, E_{TS}, products, E_P, and products after O_2-addition, E_{P-O_2}, of the reactions shown in Scheme S7 calculated relative to BCP-oxy.

Reaction	E_{TS}	E_P	E_{P-O_2}
R1	8.4	-52.3	
R2	-49.5	-69.8	
R3	-52.6	-69.5	[a]
R4	-44.0	-45.6	
R5		-94.0	
R6	-68.9	-74.2	[b]
R7	-46.8	-51.4	
R8	-50.4	-66.0	-91.4
R9	-58.4	-78.4	-88.8
R10		-88.2	
R11	-54.6	-66.9	
R12	-43.4	-56.6	
R13	-47.5	-69.7	-97.9
R14	-51.7	-84.6	-85.6

[a] Corresponds to R5-P
[b] Corresponds to R10-P

The possible unimolecular reactions of $C_6H_7O_4$-yl is outlined in Scheme S7 and modeled with Rice-Ramsperger-Kassel-Marcus Master Equation methods (RRKM-ME) using the Master Equation Solver for Multi Energy-well Reactions (MESMER) version 6.0.[50] The stationary points used for the simulations are the lowest-energy conformers at the ωB97X-D/6-311+G(d,p) level and the modeling is based on energies at that level. This level is selected because the TS for the 1,5 alkoxy H-shift from *trans*-$C_6H_7O_4$-oxy could not be optimized with the aug-cc-pVTZ basis set (a scan suggests that the reaction is barrierless at that level). For products of decomposition reactions, the optimized IRC end-point conformer is used. For products of O_2-addition reaction, an arbitrary conformer is used rather than the lowest-energy conformers but this is not expected to impact the simulations as these are modelled as sinks. The modeling starts from BCP-oxy, but includes only ring-breakage to the *trans*-$C_6H_7O_4$-oxy, as the branching between the *trans* and *cis* $C_6H_7O_4$-oxy isomers is unknown. If one assumes *cis*-$C_6H_7O_4$-oxy as the only isomer produced from $C_6H_7O_4$-oxy

ring-breakage, the yields reported here represent the upper limits from BCP-oxy channel.

The following parameters are used for the modeling:

- $k(R\cdot+O_2) = 1.4\times10^{-11}$ cm^3 $molecule^{-1}$ s^{-1}. Based on experimental results for cyclohexyl at 298 K.[51] This value may be an upper limit as most of the alkyl radicals are delocalized and thus likely react slower.

- Atmospheric O_2 concentration of 5.36×10^{18} molecules cm^{-3}.

- Exponential energy decay with an average energy transfer per collision (ΔE_{down} = 278.89 cm^{-1}) based on experimental results for toluene with N_2 as the bath gas.[52]

- Lennard-Jones parameters for the benzene-derived species: $\sigma = 5.92$ Å and $\varepsilon/k = 410$ K. Values for toluene.[52,53]

- Bath gas = N_2 ($\sigma = 3.919$ Å, $\varepsilon/k_B = 91.85$ K).[54]

- P = 760 Torr, T = 298.15 K

- Grain size = 100 cm^{-1} and automatically determined upper limit to the span of energy grains with threshold population of 1×10^{-15}. A test done with a grain size of 75 cm^{-1} for a subsystem yielded negligible differences suggesting that a grain size of 100 cm^{-1} is suitable.

- Numerical precision = qd. This was found to be necessary for reliable modeling.

Simulation 1

To assess if any of the reversible unimolecular reactions in Scheme S7 are negligible, we did a RRKM-ME modeling of the system treating the products of the unimolecular reaction (excluding R3 and R6) as sinks. The results indicate that the OH H-shifts abstracting the H from a hydroxy group (R7 and R12) are negligible (Table S7) and these are excluded from the final simulation.

Table S7: Final fractional populations in the RRKM modelling of the system outlined in Scheme S7 without the dashed O_2 addition steps and treating all products as sinks. The species with a final fractional population of zero are the only ones not treated as sinks. Treating the products of the reversible H-shifts as sinks likely leads to (potentially significant) overestimation of their importance, see Table S8 for the corresponding results when not treating them as sinks.

Compound	Final Fractional Population
BCP-oxy	0.0
R1-P: *trans*-$C_6H_7O_4$-oxy	0.0
R2-P	5.6×10^{-1}
R3-P: $C_6H_7O_4$-yl (bent)	0.0
R4-P	1.1×10^{-1}
R5-P	1.7×10^{-4}
R6-P: $C_6H_7O_4$-yl (straight)	0.0
R7-P	1.4×10^{-3}
R8-P	1.6×10^{-2}
R9-P	9.9×10^{-2}
R10-P	8.7×10^{-4}
R11-P	2.0×10^{-1}
R12-P	8.4×10^{-4}
R13-P	6.9×10^{-3}
R14-P	1.1×10^{-2}

Simulation 2

Treating the unimolecular H-shifts as sinks likely leads to an overestimation of their importance, as they are reversible. Therefore, we redid the modeling allowing these reactions to be reversible and instead adding an irreversible O_2-addition step as shown by the dashed arrows in Scheme S7. The results from this simulation are shown in Table S8, Figure S14. and summarized in Scheme S8. This MESMER modeling suggests that about 56% of the *trans*-$C_6H_7O_4$-oxy undergoes the dissociation reaction (R2) leading to butenedial and glyoxal and about 44% undergoes the 1,5-aldehydic H-shift to form $C_6H_7O_4$-yl. This result is largely in overall agreement with the results presented by Wang et al.[14], if the $C_6H_7O_4$-oxy in Wang et al.[14] refers to the *trans* isomer. Regarding the reactions of $C_6H_7O_4$-yl, Wang et al.[14] suggests that it exclusively decomposes to ketene-enol, but our calculation suggests that a fraction of $C_6H_7O_4$-yl undergoes CO-loss (R4), which constitutes 14% of

the total product from the reactions of *trans*-$C_6H_7O_4$-oxy (Table S8). Thus, CO-loss is an important pathway. The CO-loss is accompanied by a product with five carbon atoms, which provides an alternative pathway to produce lower-carbon-containing products. Zaytsev et al.[55] detected a plethora of C6 products and C8 products in the oxidation of toluene (C7) and 1,2,4-trimethylbenzne (C9), respectively, and noted their formation mechanism is unclear. A few percent of $C_6H_7O_4$-yl undergoes some H-shifts, which could lead to the formation of HOMs.

Table S8: Final fractional populations in the RRKM modelling of the system outlined in Scheme S7 excluding R7 and R12. Decomposition reactions and O_2-additions are modelled as being irreversible. The time profile of the species population is shown in Figure S14. Major pathways are highlighted in bold.

Compound	Final Fractional Population
BCP-oxy	0.0
R1-P: *trans*-$C_6H_7O_4$-oxy	0.0
R2-P	$\mathbf{5.6\times10^{-1}}$
R3-P: $C_6H_7O_4$-yl (bent)	0.0
R4-P	$\mathbf{1.4\times10^{-1}}$
R5-P	2.6×10^{-4}
R6-P: $C_6H_7O_4$-yl (straight)	0.0
R8-P	0.0
R8-P-O_2	2.1×10^{-4}
R9-P	0.0
R9-P-O_2	1.2×10^{-2}
R10-P	1.7×10^{-3}
R11-P	$\mathbf{2.7\times10^{-1}}$
R13-P	0.0
R13-P-O_2	2.8×10^{-3}
R14-P	0.0
R14-P-O_2	1.3×10^{-2}

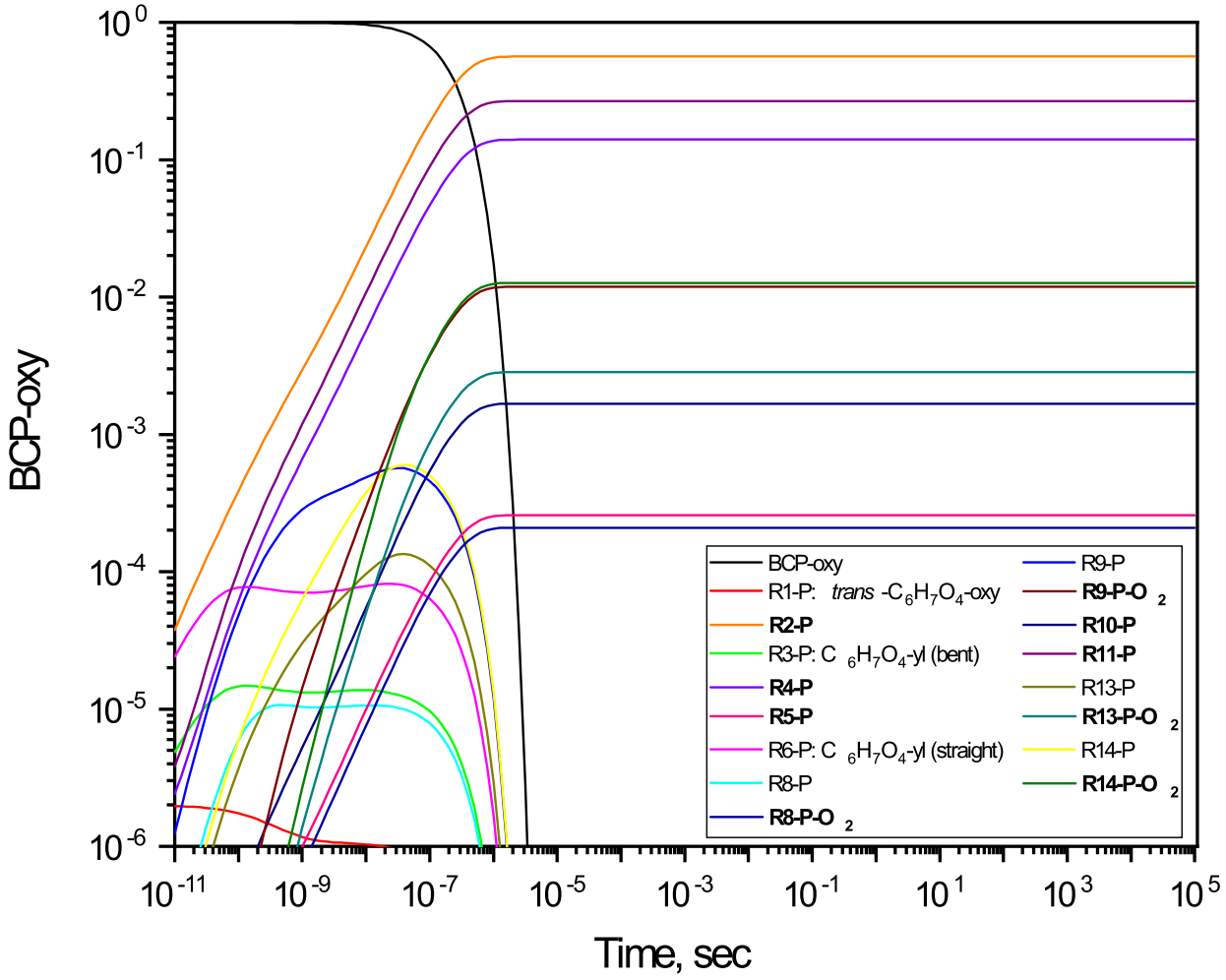

Figure S14: Fractional product population as a function of time in the RRKM-ME modeling of the system shown in Scheme S7 excluding R7 and R12. Products of decomposition reactions and O_2-additions (highlighted in bold in the legend) are treated as sinks. The final product distribution is presented also in Table S8.

The theoretical findings are summarized in Scheme S8. Our theoretical study suggests that the decomposition of BCP-oxy produces both *cis* and *trans* $C_6H_7O_4$-oxy isomers (Scheme S6). The *cis* isomer dominantly undergoes decomposition, but the *trans* isomer can undergo both decomposition and 1,5-aldehydic H-shift (Table S5). However, the distribution of *cis* and *trans* isomers is unclear and the isomer-specific chemistry is not discussed in Wang et al.[14]. Further, theoretical calculation suggests that about 56% of the *trans*-$C_6H_7O_4$-oxy undergoes the dissociation reaction leading to butenedial and glyoxal and about 44% undergoes the 1,5-aldehydic H-shift to form $C_6H_7O_4$-yl (Table S8). This is largely in overall

agreement with the results presented by Wang et al.[14]. In contrast to Wang et al.[14] which suggested that $C_6H_7O_4$-yl exclusive decomposes to ketene-enol, we find that about 30% of $C_6H_7O_4$-yl undergoes CO-loss and an additional 7% undergoes other reactions. The CO-loss constitutes 14% of the total product from the reactions of *trans*-$C_6H_7O_4$-oxy (Table S8).

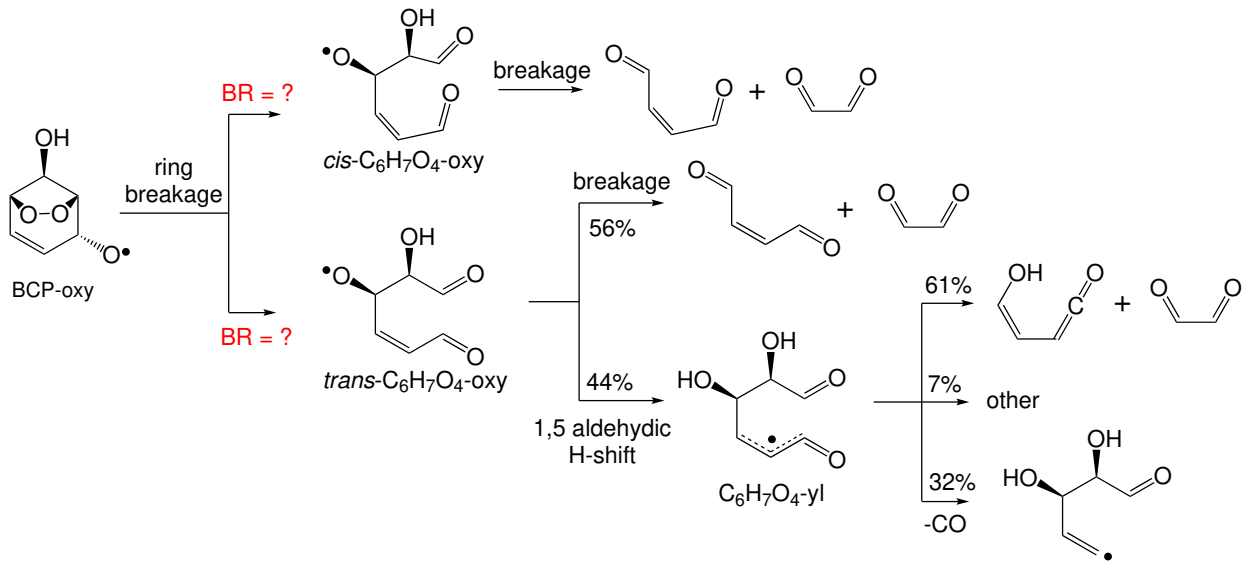

Scheme S8: Summary of key theoretical findings on BCP-oxy chemistry.

Theoretical yield of fumaraldehydic acid

Under low NOx conditions, the theoretical yield of fumaraldehydic acid (Y_{FAA}) is equal to the product of branching ratios along its formation pathway (Scheme S9 and Eqn. S18)

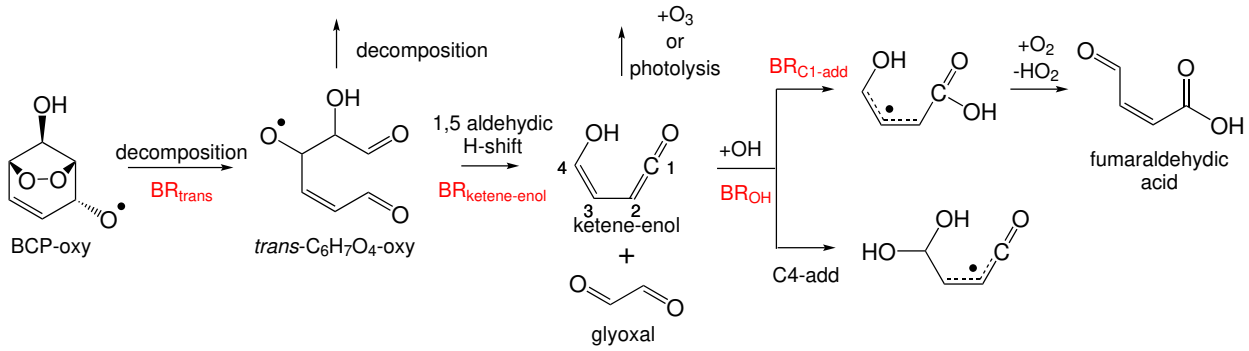

Scheme S9: Simplified formation mechanism of fumaraldehydic acid from the 1,5-aldehydic H-shift of BCP-oxy based on Wang et al.[14].

$$Y_{FAA} = Y_{BCP-oxy} \cdot BR_{trans} \cdot BR_{ketene-enol} \cdot BR_{OH} \cdot BR_{C1-add} \quad (18)$$

where $Y_{BCP-oxy}$ represents the yield of BCP-oxy, BR_{trans} represents the branching ratio for BCP-oxy decomposition to produce *trans*-$C_6H_7O_4$-oxy isomer, $BR_{ketene-enol}$ represents the branching ratio for ketene-enol formation from *trans*-$C_6H_7O_4$-oxy, BR_{OH} represents the branching ratio for ketene-enol undergoing OH addition, and BR_{C1-add} represents branching ratio for OH addition to the ketene carbon connected to the oxygen (Scheme S9). $Y_{BCP-oxy}$ is roughly 47% under low NO conditions (i.e., NO $<$ a few ppbv) as discussed in the main text. BR_{trans} is unknown and assumed to be 50%. $BR_{ketene-enol}$ is theoretically calculated to be 0.27 (44% $\times$ 61% in Scheme S8). BR_{OH} is estimated to be 0.8 based on the [OH] (1.75×10^8 molecule cm^{-3}), [O_3] ($\sim$50 ppb), and $j_{ketene-enol}$ (3.2×10^{-3} s^{-1}) in low NOx experiments (Expts. 8 and 9) in this study. BR_{C1-add} is theoretically calculated to be 0.64 by Wang et al.[14]. Therefore, the theoretical yield of fumaraldehydic acid (FAA) under low NOx conditions is 3.5%.

Wang et al.[14] used formic acid measurement in an laboratory (E)-butenedial photooxidation experiment to evaluate the theoretically calculated fate of ketene-enol. However, the fate of $C_6H_7O_4$-oxy is not experimentally accessed in that study. Here, we select fumaraldehydic acid to constrain the fate of $C_6H_7O_4$-oxy, because it is a unique product following the $C_6H_7O_4$-oxy H-shift and subsequent $C_6H_7O_4$-yl decomposition. Formic acid is also measured in this study, but not used in this analysis because formic acid could be formed from the illumination of the chamber walls and unknown formation pathways.

S11: C-oxy chemistry

C-oxy is subject to both ring-closure and ring-breakage. The ratio of two pathways is stereo-specific. The barrier heights of ring-closure and ring-breakage are calculated to be the same for *ortho-anti*-C-oxy (Table S9), suggesting both channels are likely of comparable

importance. For *ortho-syn*-C-oxy, however, the barrier height of ring-closure is more than 4 kcal mol^{-1} lower than that of ring-breakage, suggesting ring-closure is likely the dominant fate of *ortho-syn*-C-oxy.

The ring-breakage of C-oxy, followed by O_2 addition and HO_2 elimination, produces 2,4-hexadienedial (muconaldehyde, $C_6H_6O_2$). GC-CIMS resolves two major peaks in the chromotogram of *m/z* 195 ($C_6H_6O_2 \cdot CF_3O^-$)(Figure S6) and the H/D exchange analysis reveals that neither peak has any exchangeable H, consistent with the chemical identify of 2,4-hexadienedial. 2,4-hexadienedial has Z,Z-, E,Z-, and E,E-isomers. Klotz et al.[56] showed that Z,Z-isomer thermally isomerize to the E,Z-isomer with a lifetime of 13 min, a time scale similar to the oxidation time and GC sampling in this study. Thus, the two major peaks resolved by GC-CIMS likely represent E,Z- and E,E isomers.

The total yield of 2,4-hexadienedial (i.e., sum of both isomers) increases with shorter $\tau_{RO_2,bimolecular}$ (Figure S7), consistent with C-oxy chemistry as its major source. At the shortest $\tau_{RO_2,bimolecular}$ (10^{-3} s) in this study, the yield is 17%, but still does not reach a plateau, as a result of the fast unimolecular reactions of C-peroxy. At the longest $\tau_{RO_2,bimolecular}$ (2 s), the yield is low (1%), but non-zero. This is unexpected as C-peroxy predominantly undergoes unimolecular reactions and the formation of C-oxy is negligible under this condition. This non-zero yield implies that some unknown pathway produces 2,4-hexadienedial without the involvement of NO.

Table S9: ωB97X-D/aug-cc-pVTZ barrier heights of the ring-breakage and ring-closure reactions for C-oxy isomers (kcal mol^{-1}).

Isomer	ring-breakage	ring-closure
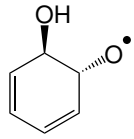 *ortho-anti*-C-oxy	2.3	2.3
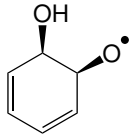 *ortho-syn*-C-oxy	5.0	0.8

S12: Literature values of glyoxal yields

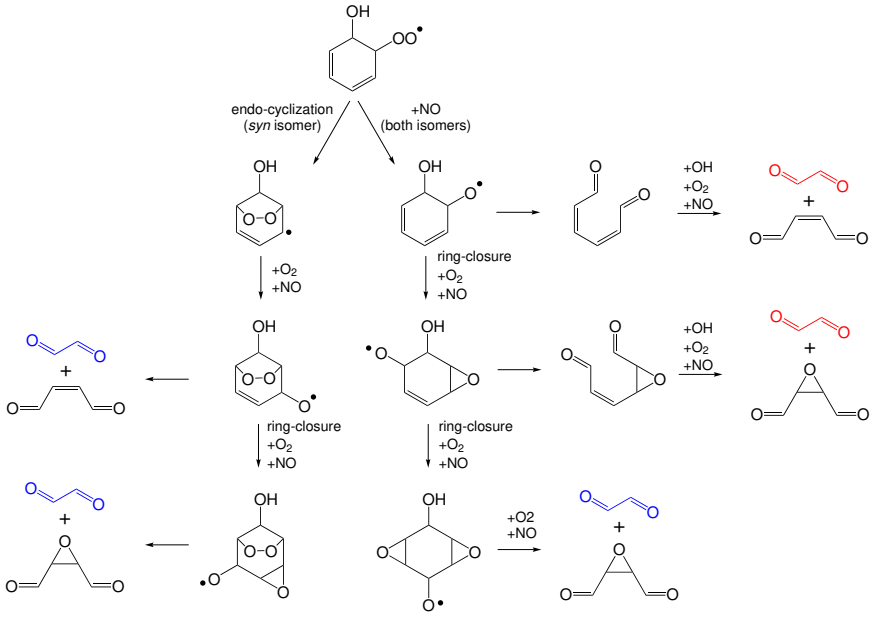

Scheme S10: Formation pathways of glyoxal. Primary formation is marked blue and secondary formation is marked red.

Table S10 summarizes literature glyoxal yields and corresponding experimental conditions. To obtain the RO_2 bimolecular lifetime and hence compare the literature data in Figure 4, we input the initial concentrations of species, photolysis rate, oxidation time, as reported by

each study, into the kinetic model described in section S5.

Table S10: Reported glyoxal yields at room temperature and pressure.

reference	yield (%)	benzene[a] (ppm)	NO[a] (ppb)	NO_2[a] (ppb)	OH source & conc. (ppm)	j_{NO_2} ($\times 10^{-3}$ s^{-1})	ox. time (min)
Tuazon[57]	21±2	10	4.9×10^3	0	CH_3ONO (9.8)	4.4[b]	3
Volkamer[58]	35±10	10	80	40	HONO (0.08)	2.5	85
Berndt[59]	29±10	120-180	18-58	0	CH_3ONO (0.41)	4.7	10.4
Alvarez[60]	42±3	2	6	20	HONO (0.034)	6.7	30
Alvarez[60]	36±2	39	14	37	HONO (0.064)	6.5	30

[a] The concentrations refer to initial values before oxidation.
[b] A biacetyl photolysis rate of 1.25×10^{-4} s^{-1} is reported for 25 kW xenon arc. The j_{NO_2} is difficult to estimate, but assumed to be the same as this study.

References

(1) Taylor, W. D.; Allston, T. D.; Moscato, M. J.; Fazekas, G. B.; Kozlowski, R.; Takacs, G. A. Atmospheric Photo-Dissociation Lifetimes for Nitromethane, Methyl Nitrite, and Methyl Nitrate. *Int. J. Chem. Kinet.* **1980**, *12*, 231–240.

(2) Crounse, J. D.; McKinney, K. A.; Kwan, A. J.; Wennberg, P. O. Measurement of Gas-Phase Hydroperoxides by Chemical Ionization Mass Spectrometry. *Analytical Chemistry* **2006**, *78*, 6726–6732.

(3) Clair, J. M. S.; McCabe, D. C.; Crounse, J. D.; Steiner, U.; Wennberg, P. O. Chemical ionization tandem mass spectrometer for the in situ measurement of methyl hydrogen peroxide. *Review of Scientific Instruments* **2010**, *81*, 094102.

(4) Paulot, F.; Crounse, J. D.; Kjaergaard, H. G.; Kroll, J. H.; Seinfeld, J. H.; Wennberg, P. O. Isoprene photooxidation: new insights into the production of acids and organic nitrates. *Atmospheric Chemistry and Physics* **2009**, *9*, 1479–1501.

(5) Garden, A. L.; Paulot, F.; Crounse, J. D.; Maxwell-Cameron, I. J.; Wennberg, P. O.;

Kjaergaard, H. G. Calculation of conformationally weighted dipole moments useful in ion–molecule collision rate estimates. *Chem. Phys. Lett.* **2009**, *474*, 45–50.

(6) Su, T.; Chesnavich, W. J. Parametrization of the ion–polar molecule collision rate constant by trajectory calculations. *J. Chem. Phys.* **1982**, *76*, 5183–5185.

(7) Smith, D.; Adams, N. G.; Miller, T. M. A laboratory study of the reactions of N+, N2+, N3+, N4+, O+, O2+, and NO+ ions with several molecules at 300K. *J. Chem. Phys.* **1978**, *69*, 308–318.

(8) Koss, A. R.; Warneke, C.; Yuan, B.; Coggon, M. M.; Veres, P. R.; de Gouw, J. A. Evaluation of NO+ reagent ion chemistry for online measurements of atmospheric volatile organic compounds. *Atmos. Meas. Tech.* **2016**, *9*, 2909–2925.

(9) Francis, G. J.; Milligan, D. B.; McEwan, M. J. Gas-Phase Reactions and Rearrangements of Alkyl Esters with H3O+, NO+, and O2•+: A Selected Ion Flow Tube Study. *J. Phys. Chem. A* **2007**, *111*, 9670–9679.

(10) Španél, P.; Smith, D. Selected ion flow tube studies of the reactions of H3O+, NO+, and O2+ with several aromatic and aliphatic hydrocarbons. *Int. J. Mass. Spectrom.* **1998**, *181*, 1–10.

(11) Kroll, J. H.; Ng, N. L.; Murphy, S. M.; Varutbangkul, V.; Flagan, R. C.; Seinfeld, J. H. Chamber studies of secondary organic aerosol growth by reactive uptake of simple carbonyl compounds. *Journal of Geophysical Research-Atmospheres* **2005**, *110*.

(12) Guimbaud, C.; Catoire, V.; Bergeat, A.; Michel, E.; Schoon, N.; Amelynck, C.; Labonnette, D.; Poulet, G. Kinetics of the reactions of acetone and glyoxal with O2+ and NO+ ions and application to the detection of oxygenated volatile organic compounds in the atmosphere by chemical ionization mass spectrometry. *Int. J. Mass. Spectrom.* **2007**, *263*, 276–288.

(13) Klotz, B.; Barnes, I.; Becker, K. H. Kinetic study of the gas-phase photolysis and OH radical reaction of E,Z- and E,E-2,4-hexadienedial. *International Journal of Chemical Kinetics* **1999**, *31*, 689–697.

(14) Wang, S.; Newland, M. J.; Deng, W.; Rickard, A. R.; Hamilton, J. F.; Muñoz, A.; Ródenas, M.; Vázquez, M. M.; Wang, L.; Wang, X. Aromatic Photo-oxidation, A New Source of Atmospheric Acidity. *Environ. Sci. Technol.* **2020**,

(15) Newland, M. J.; Rea, G. J.; Thüner, L. P.; Henderson, A. P.; Golding, B. T.; Rickard, A. R.; Barnes, I.; Wenger, J. Photochemistry of 2-butenedial and 4-oxo-2-pentenal under atmospheric boundary layer conditions. *Phys. Chem. Chem. Phys.* **2019**, *21*, 1160–1171.

(16) Atkinson, R.; Aschmann, S. M.; Carter, W. P. L.; Winer, A. M.; Pitts, J. N. Alkyl nitrate formation from the nitrogen oxide (NOx)-air photooxidations of C2-C8 n-alkanes. *J. Phys. Chem.* **1982**, *86*, 4563–4569.

(17) Saunders, S. M.; Jenkin, M. E.; Derwent, R. G.; Pilling, M. J. Protocol for the development of the Master Chemical Mechanism, MCM v3 (Part A): tropospheric degradation of non-aromatic volatile organic compounds. *Atmos. Chem. Phys.* **2003**, *3*, 161–180.

(18) Eyring, H. The Activated Complex in Chemical Reactions. *J. Chem. Phys.* **1935**, *3*, 107–115.

(19) Evans, M. G.; Polanyi, M. Some Applications of the Transition State Method to the Calculation of Reaction Velocities, Especially in Solution. *Trans. Faraday Soc.* **1935**, *31*, 875–894.

(20) Vereecken, L.; Peeters, J. The 1,5-H-shift in 1-butoxy: A case study in the rigorous implementation of transition state theory for a multirotamer system. *J. Chem. Phys.* **2003**, *119*, 5159–5170.

(21) Møller, K. H.; Otkjær, R. V.; Hyttinen, N.; Kurtén, T.; Kjaergaard, H. G. Cost-Effective Implementation of Multiconformer Transition State Theory for Peroxy Radical Hydrogen Shift Reactions. *J. Phys. Chem. A* **2016**, *120*, 10072–10087.

(22) Eckart, C. The Penetration of a Potential Barrier by Electrons. *Phys. Rev.* **1930**, *35*, 1303–1309.

(23) Becke, A. D. Density-Functional Thermochemistry. III. The Role of Exact Exchange. *J. Chem. Phys.* **1993**, *98*, 5648–5652.

(24) Lee, C.; Yang, W.; Parr, R. G. Development of the Colle-Salvetti Correlation-Energy Formula into a Functional of the Electron Density. *Phys. Rev. B* **1988**, *37*, 785–789.

(25) Hehre, W. J.; Ditchfield, R.; Pople, J. A. Self—Consistent Molecular Orbital Methods. XII. Further Extensions of Gaussian—Type Basis Sets for Use in Molecular Orbital Studies of Organic Molecules. *J. Chem. Phys.* **1972**, *56*, 2257–2261.

(26) Clark, T.; Chandrasekhar, J.; Spitznagel, G. W.; Schleyer, P. V. R. Efficient Diffuse Function-augmented Basis Sets for Anion Calculations. III. The 3-21+G Basis Set for First-row Elements, Li–F. *J. Comput. Chem.* **1983**, *4*, 294–301.

(27) Frisch, M. J.; Pople, J. A.; Binkley, J. S. Self-consistent Molecular Orbital Methods 25. Supplementary Functions for Gaussian Basis Sets. *J. Chem. Phys.* **1984**, *80*, 3265–3269.

(28) Frisch, M. J.; Trucks, G. W.; Schlegel, H. B.; Scuseria, G. E.; Robb, M. A.; Cheeseman, J. R.; Scalmani, G.; Barone, V.; Petersson, G. A.; Nakatsuji, H.; Li, X.; Caricato, M.; Marenich, A. V.; Bloino, J.; Janesko, B. G.; Gomperts, R.; Mennucci, B.; Hratchian, H. P.; Ortiz, J. V.; Izmaylov, A. F.; Sonnenberg, J. L.; Williams-Young, D.; Ding, F.; Lipparini, F.; Egidi, F.; Goings, J.; Peng, B.; Petrone, A.; Henderson, T.; Ranasinghe, D.; Zakrzewski, V. G.; Gao, J.; Rega, N.; Zheng, G.; Liang, W.; Hada, M.; Ehara, M.; Toyota, K.; Fukuda, R.; Hasegawa, J.; Ishida, M.; Nakajima, T.;

Honda, Y.; Kitao, O.; Nakai, H.; Vreven, T.; Throssell, K.; Montgomery, J. A., Jr.; Peralta, J. E.; Ogliaro, F.; Bearpark, M. J.; Heyd, J. J.; Brothers, E. N.; Kudin, K. N.; Staroverov, V. N.; Keith, T. A.; Kobayashi, R.; Normand, J.; Raghavachari, K.; Rendell, A. P.; Burant, J. C.; Iyengar, S. S.; Tomasi, J.; Cossi, M.; Millam, J. M.; Klene, M.; Adamo, C.; Cammi, R.; Ochterski, J. W.; Martin, R. L.; Morokuma, K.; Farkas, O.; Foresman, J. B.; Fox, D. J. Gaussian 16 Revision C.01. 2016; Gaussian Inc. Wallingford CT.

(29) Spartan '18. Wavefunction Inc., Irvine, CA.

(30) Halgren, T. A. Merck Molecular Force Field. I. Basis, Form, Scope, Parameterization, and Performance of MMFF94. *J. Comput. Chem.* **1996**, *17*, 490–519.

(31) Chai, J.-D.; Head-Gordon, M. Long-range Corrected Hybrid Density Functionals with Damped Atom-atom Dispersion Corrections. *Phys. Chem. Chem. Phys.* **2008**, *10*, 6615–6620.

(32) Dunning, T. H. Gaussian Basis Sets for Use in Correlated Molecular Calculations. I. The Atoms Boron Through Neon and Hydrogen. *J. Chem. Phys.* **1989**, *90*, 1007–1023.

(33) Kendall, R. A.; Dunning, T. H.; Harrison, R. J. Electron Affinities of the First-row Atoms Revisited. Systematic Basis Sets and Wave Functions. *J. Chem. Phys.* **1992**, *96*, 6796–6806.

(34) Werner, H.-J.; Knowles, P. J.; Knizia, G.; Manby, F. R.; Schütz, M.; Celani, P.; Györffy, W.; Kats, D.; Korona, T.; Lindh, R.; Mitrushenkov, A.; Rauhut, G.; Shamasundar, K. R.; Adler, T. B.; Amos, R. D.; Bernhardsson, A.; Berning, A.; Cooper, D. L.; Deegan, M. J. O.; Dobbyn, A. J.; Eckert, F.; Goll, E.; Hampel, C.; Hesselmann, A.; Hetzer, G.; Hrenar, T.; Jansen, G.; Köppl, C.; Liu, Y.; Lloyd, A. W.; Mata, R. A.; May, A. J.; McNicholas, S. J.; Meyer, W.; Mura, M. E.; Nicklass, A.; O'Neill, D. P.; Palmieri, P.; Peng, D.; Pflüger, K.; Pitzer, R.; Reiher, M.; Shiozaki, T.;

Stoll, H.; Stone, A. J.; Tarroni, R.; Thorsteinsson, T.; Wang, M. MOLPRO, version 2012.1, a package of ab initio programs. 2012; see http://www.molpro.net.

(35) Watts, J. D.; Gauss, J.; Bartlett, R. J. Coupled-Cluster Methods with Noniterative Triple Excitations for Restricted Open-shell Hartree-Fock and Other General Single Determinant Reference Functions. Energies and Analytical Gradients. *J. Chem. Phys.* **1993**, *98*, 8718–8733.

(36) Adler, T. B.; Knizia, G.; Werner, H.-J. A Simple and Efficient CCSD(T)-F12 Approximation. *J. Chem. Phys.* **2007**, *127*, 221106.

(37) Knizia, G.; Adler, T. B.; Werner, H.-J. Simplified CCSD(T)-F12 Methods: Theory and Benchmarks. *J. Chem. Phys.* **2009**, *130*, 054104.

(38) Werner, H.-J.; Knizia, G.; Manby, F. R. Explicitly Correlated Coupled Cluster Methods with Pair-specific Geminals. *Mol. Phys.* **2011**, *109*, 407–417.

(39) Peterson, K. A.; Adler, T. B.; Werner, H.-J. Systematically Convergent Basis Sets for Explicitly Correlated Wavefunctions: The Atoms H, He, B–Ne, and Al–Ar. *J. Chem. Phys.* **2008**, *128*, 084102.

(40) Møller, K. H.; Bates, K. H.; Kjaergaard, H. G. The Importance of Peroxy Radical Hydrogen-Shift Reactions in Atmospheric Isoprene Oxidation. *J. Phys. Chem. A* **2019**, *123*, 920–932.

(41) Raoult, S.; Rayez, M. T.; Rayez, J. C.; Lesclaux, R. Gas phase oxidation of benzene: Kinetics, thermochemistry and mechanism of initial steps. *Phys. Chem. Chem. Phys.* **2004**, *6*, 2245–2253.

(42) Glowacki, D. R.; Wang, L.; Pilling, M. J. Evidence of Formation of Bicyclic Species in the Early Stages of Atmospheric Benzene Oxidation. *J. Phys. Chem. A* **2009**, *113*, 5385–5396.

(43) Olivella, S.; Solé, A.; Bofill, J. M. Theoretical Mechanistic Study of the Oxidative Degradation of Benzene in the Troposphere: Reaction of Benzene-HO Radical Adduct with O2. *J. Chem. Theory Comput* **2009**, *5*, 1607–1623.

(44) Lay, T. H.; Bozzelli, J. W.; Seinfeld, J. H. Atmospheric Photochemical Oxidation of Benzene: Benzene + OH and the Benzene-OH Adduct (Hydroxyl-2,4-cyclohexadienyl) + O2. *J. Phys. Chem.* **1996**, *100*, 6543–6554.

(45) Klotz, B.; Volkamer, R.; Hurley, M. D.; Andersen, M. P. S.; Nielsen, O. J.; Barnes, I.; Imamura, T.; Wirtz, K.; Becker, K.-H.; Platt, U.; Wallington, T. J.; Washida, N. OH-initiated oxidation of benzene Part II.Influence of elevated NO concentrations. *Phys. Chem. Chem. Phys.* **2002**, *4*, 4399–4411.

(46) Knispel, R.; Koch, R.; Siese, M.; Zetzsch, C. Adduct Formation of OH Radicals with Benzene, Toluene, and Phenol and Consecutive Reactions of the Adducts with NOx and O2. *Berichte der Bunsengesellschaft für physikalische Chemie* **1990**, *94*, 1375–1379.

(47) Teng, A. P.; Crounse, J. D.; Wennberg, P. O. Isoprene Peroxy Radical Dynamics. *J. Am. Chem. Soc.* **2017**, *139*, 5367–5377.

(48) Motta, F.; Ghigo, G.; Tonachini, G. Oxidative Degradation of Benzene in the Troposphere. Theoretical Mechanistic Study of the Formation of Unsaturated Dialdehydes and Dialdehyde Epoxides. *J. Phys. Chem. A* **2002**, *106*, 4411–4422.

(49) Wang, L.; Wu, R.; Xu, C. Atmospheric Oxidation Mechanism of Benzene. Fates of Alkoxy Radical Intermediates and Revised Mechanism. *J. Phys. Chem. A* **2013**, *117*, 14163–14168.

(50) Glowacki, D. R.; Liang, C.-H.; Morley, C.; Pilling, M. J.; Robertson, S. H. MESMER: An Open-Source Master Equation Solver for Multi-Energy Well Reactions. *J. Phys. Chem. A* **2012**, *116*, 9545–9560.

(51) Wu, D.; Bayes, K. D. Rate constants for the reactions of isobutyl, neopentyl, cyclopentyl, and cyclohexyl radicals with molecular oxygen. *Int. J. Mass. Spectrom.* **1986**, *18*, 547–554.

(52) Hippler, H.; Troe, J.; Wendelken, H. J. Collisional deactivation of vibrationally highly excited polyatomic molecules. II. Direct observations for excited toluene. *J. Chem. Phys.* **1983**, *78*, 6709–6717.

(53) Mourits, F.; Rummens, F. A critical evaluation of Lennard–Jones and Stockmayer potential parameters and of some correlation methods. *Can. J. Chem* **1977**, *55*, 3007–3020.

(54) Cuadros, F.; Mulero, A.; Cachadiña, J.; Ahumada, W. A New Procedure for Determining Lennard-Jones Interaction Parameters. *Int. Rev. Phys. Chem.* **1995**, *14*, 205–213.

(55) Zaytsev, A.; Koss, A. R.; Breitenlechner, M.; Krechmer, J. E.; Nihill, K. J.; Lim, C. Y.; Rowe, J. C.; Cox, J. L.; Moss, J.; Roscioli, J. R.; Canagaratna, M. R.; Worsnop, D. R.; Kroll, J. H.; Keutsch, F. N. Mechanistic study of the formation of ring-retaining and ring-opening products from the oxidation of aromatic compounds under urban atmospheric conditions. *Atmos. Chem. Phys.* **2019**, *19*, 15117–15129.

(56) Klotz, B. G.; Bierbach, A.; Barnes, I.; Becker, K. H. Kinetic and Mechanistic Study of the Atmospheric Chemistry of Muconaldehydes. *Environ. Sci. Technol.* **1995**, *29*, 2322–2332.

(57) Tuazon, E. C.; MacLeod, H.; Atkinson, R.; Carter, W. P. L. .alpha.-Dicarbonyl yields from the NOx-air photooxidations of a series of aromatic hydrocarbons in air. *Environ. Sci. Technol.* **1986**, *20*, 383–387.

(58) Volkamer, R.; Platt, U.; Wirtz, K. Primary and Secondary Glyoxal Formation from

Aromatics: Experimental Evidence for the Bicycloalkyl Radical Pathway from Benzene, Toluene, and p-Xylene. *J. Phys. Chem. A* **2001**, *105*, 7865–7874.

(59) Berndt, T.; Böge, O. Formation of phenol and carbonyls from the atmospheric reaction of OH radicals with benzene. *Phys. Chem. Chem. Phys.* **2006**, *8*, 1205–1214.

(60) Gómez Alvarez, E.; Viidanoja, J.; Muńoz, A.; Wirtz, K.; Hjorth, J. Experimental Confirmation of the Dicarbonyl Route in the Photo-oxidation of Toluene and Benzene. *Environ. Sci. Technol.* **2007**, *41*, 8362–8369.